Optical Properties of Reduced Graphene Oxide

Insights from *ab initio* and hybrid density functional theory

Mark James LUNDIE

School of Computing, Science and Engineering
University of Salford, Salford, UK

Submitted in Partial Fulfilment of the Requirements
of the Degree of Doctor of Philosophy, March 2016

CONTENTS

LIST OF FIGURES

LIST OF TABLES

ACKNOWLEDGEMENTS

I would like to express my sincere gratitude to my supervisor Prof. Stanko Tomić for his continued support, advice, and patience. Heartfelt thanks are also due to my co-supervisor Prof. Ian Morrison for his guidance and assistance, which have been of continual and great help.

I am most grateful for the collaboration and kindness of Dr. Željko Šljivančanin, from whom I have learned a great deal in the past three years. Dr. Leonardo Bernasconi of STFC Rutherford Appleton Laboratory has also offered invaluable assistance with some technicalities of the CRYSTAL code, which I greatly appreciate.

I must express my gratitude to Tom Walsh and Dr. Jacek Miloszewski, both of whom are a pleasure to work with and I am glad to be able to call friends.

I would also like to extend my sincerest thanks to Dr. Graham McDonald, whose advice when choosing between PhD offers and subsequently embarking on my PhD studies was invaluable.

I will always be grateful for the kindness and encouragment of Bruce Lewis, not to mention his dry sense of humour.

The continued support of my parents, Jim and Linda, and brother Michael, has helped me through the harder times. Receiving my mother's messages of encouragement never fails to lift my spirits. She always seems to know when I need it most.

Words cannot express how much I appreciate the love, support, and encouragement of my wife Liz. Her confidence and belief in me have kept me going even when I have lost my own. I also appreciate the sacrifices she has made while I pursue my passion. I sincerely look forward to being able to make it up to her.

Finally, I would like to thank all of the people I have not been able to mention personally, especially the staff of the Physics department, the college support team and many of my fellow PhD students of the school of computing, science and engineering.

DECLARATION

Chapter 5 contains results and analysis which form the basis of two papers published in collaboration with Dr. Željko Šljivančanin of the Vinča Institute of Nuclear Sciences, Serbia, and Prof. Tomić. All results presented are from my own calculations, unless explicitly stated otherwise.

LIST OF PUBLICATIONS

[1] M. J. Lundie, S. Tomić, and Ž. Šljivančanin. "Ab initio study of structural and electronic properties of partially reduced graphene oxide". In: *Phys. Scr.* T162 (2014), p. 014019.

[2] M. Lundie, Ž. Šljivančanin, and S. Tomić. "Analysis of energy gap opening in graphene oxide". In: *J. Phys. Conf. Ser.* 526 (2014), p. 012003.

[3] M. Lundie and S. Tomić. "Ab initio parameterisation of the 14 band k·p Hamiltonian: Zincblende study". In: *J. Phys. Conf. Ser.* 526 (2014), p. 012004.

[4] M. Lundie, Ž. Šljivančanin, and S. Tomić. "Electronic and optical properties of reduced graphene oxide". In: *J. Mater. Chem. C* 3 (2015), pp. 7632–7641.

[5] M. Lundie, Ž. Šlivančanin, and S. Tomić. "Absorption characteristics of reduced graphene oxide: Application to TCO and solar cells active region". In: *Photovoltaic Specialist Conference (PVSC), 2015 IEEE 42nd*. IEEE. 2015, pp. 1–4.

ABBREVIATIONS

GO	graphene oxide
rGO	reduced graphene oxide
QD	quantum dot
GQD	graphene quantum dot
GOQD	graphene oxide quantum dot
DFT	density functional theory
TD-DFT	time-dependent density functional theory
LDA	local density approximation
GGA	generalised gradient approximation
GTO	Gaussian-type orbital
BSSE	basis set superposition error
PW	plane wave
PAW	projector augmented wave
IBZ	irreducible Brillouin zone
ML	monolayer
HOMO	highest occupied molecular orbital
LUMO	lowest unoccupied molecular orbital
PL	photoluminescence

ABSTRACT

Graphene, despite its many remarkable material properties, is fundamentally limited for many photonic and microelectronic applications due to its semi-metallic nature. Chemical functionalisation of graphene affords one route toward opening an energy gap, potentially extending its utility to these areas. Graphene oxide strongly absorbs in the ultraviolet range and reduction by various chemical treatments has been demonstrated to shift the absorption peak toward the visible spectrum. Photoluminescence emission has also been observed across the spectrum from ultraviolet to infrared, further suggesting the possibility of tuning optical properties. However, such methods produce highly defective graphene oxide, with hydroxyl, carboxyl, and carbonyl moieties being left behind in addition to the desirable epoxy functional groups. Considerable damage to the graphene sub-lattice is also caused. More recently, chemical deposition of atomic oxygen on graphene has been shown to form epoxy functional groups on graphene without causing this damage. Ab initio and hybrid density functional theory and time-dependent density theory studies of graphene oxide and reduced graphene oxide are carried out to investigate its structural, electronic, and optical properties. Patterned removal of oxygen to form graphene quantum dots embedded in the graphene oxide lattice is shown to permit tuning of the energy gap and optical absorption from ultraviolet through to infrared wavelengths, with long calculated radiative relaxation times. A simple relationship between the predicted gap and size of the most symmetric quantum dot structures, which are also the most thermodynamically stable, is demonstrated.

1

INTRODUCTION

> *If, in some cataclysm, all of scientific knowledge were to be destroyed, and only one sentence passed on to the next generation of creatures, what statement would contain the most information in the fewest words? I believe it is the atomic hypothesis that all things are made of atoms - little particles that move around in perpetual motion, attracting each other when they are a little distance apart, but repelling upon being squeezed into one another. In that one sentence, you will see, there is an enormous amount of information about the world, if just a little imagination and thinking are applied.*
>
> Richard P. Feynman

GRAPHENE AND ITS MODIFICATION

The rapid development of technology in fields as diverse as microelectronics, photonics, and automotive engineering, to name but a few, has led to the development and discovery of many novel materials in recent decades. Of these new materials few, if any, are as celebrated and have achieved such levels of attention as graphene [1, 2]. Its two-dimensional network of sp^2 hybridised bonds lend it exceptional tensile strength, while the matrix of π bonds formed by the $2p_z$ orbitals contribute unparalleled electrical and

thermal conductivity [3, 4]. Although optically quite transparent due to its consisting of a single atomic layer, it is reported to absorb approximately 2.3% of incident white light [5]. In spite of this, the fact that it is a zero band gap semiconductor, or semimetal, poses a challenge to its utility to photonics applications [6]. The lack of energy gap also limits applications to micro- and nanoelectronics without modification, where its high carrier mobility make it highly desirable for the construction of transistors.

As such, since its original isolation by means of micromechanical exfoliation[1] over a decade ago, considerable attention has been placed on the manipulation of its electronic structure in order to open a gap. A wide array of methods are employed towards this end, but the aim common to the majority of these is the disruption of the π bonding network. One common method by which this can be achieved is nanostructuring to form graphene nanoribbons (GNR) [7] or quantum dots (GQD) [8], in which quantum confinement effects lead to the creation of a finite gap proportional to the width or diameter. A promising alternative is the covalent modification of graphene by functionalisation with atoms such as hydrogen, fluorine and oxygen [9, 10]. Such modification can be used to open and tune the energy gap by rehybridising some or all of the C-C bonds to sp^3. In this manner, tuning of the gap can be effected by manipulating the ratio of sp^3 to sp^2 bonds. It is a combination of these methods, namely the patterned epoxy functionalisation of graphene by adsorption of atomic oxygen, on which this study is focused.

The potential applications of graphene oxide (GO) and reduced graphene oxide (rGO) are many and varied. A number of these are of special relevance and importance in relation to the drive for efficient and environmentally-

1 The infamous "Scotch tape" method".

friendly energy production and storage. For example, GO can be employed as a photocatalyst [11] for the production of hydrogen from water-splitting [12], or the production of hydrocarbon fuels [13]. It can also be employed in the production of photovoltaic (PV) solar cells [14]. RGO has been recently used to create reliable solid state supercapacitors [15]. As an interesting aside, GO even has applications to medical imaging and cancer therapy [16].

DENSITY FUNCTIONAL THEORY

Kohn-Sham density functional theory (DFT) is a widely used and extremely successful method for performing *ab initio* calculations in quantum chemistry and molecular and condensed matter physics. It is capable of the quantitative prediction of a wide range of chemical and material properties, with ever increasing accuracy and precision [17].

However, *ab initio* DFT is of limited use for the study of optical properties as it systematically underestimates the energy gap, which underpins these properties. This can be improved upon by the use of hybrid functionals, in which a fraction of exact exchange energy calculated in an analogue to the Hartree-Fock formalism, is incorporated. Although this solution is not perfect, it can and has been successfully used for the accurate prediction of the electronic and optical properties of many semiconductor and oxide materials [18, 19].

By means of *ab initio* DFT, hybrid DFT and time-dependent density functional theory (TD-DFT) calculations the structural, electronic and optical properties of fully oxidised graphene, or GO, are analysed. The effects on the properties by the formation of graphene quantum dots of increas-

ing size embedded in a GO super-lattice are then investigated. The dots are formed by the patterned removal of O adatoms to form regions of sp^2 bonded graphene embedded in the sp^3 network of the super-lattice.

The decision to use hybrid functionals is justified by the application of the methodology to some common III-V, including III-nitride, semiconductors and subsequent comparison to experimental data. The methodology used throughout has the benefit of being much more computationally efficient than many body methods such as the GW approximation, therefore allowing its extension to the large supercells of $\sim$150 atoms required to study the GO/GQD systems.

OUTLINE OF THESIS

Chapter 2 contains a short overview of some of the most important properties of graphene, before briefly considering the hydrogenation of graphene for the modification of its electronic properties. A detailed review of the literature on oxidised graphene is then given, highlighting important experimental and theoretical research into its structural, electronic, and optical properties and its application to photonics devices.

Chapter 3 provides an overview of DFT and TD-DFT, and highlights the areas of greatest importance to this work. In particular, a review of hybrid density functionals and the successes (and limitations) of their use in calculating energy gaps and optical properties is made.

Chapter 4 details the methodology employed in all simulations, explaining how optimal computational parameters were determined and basis sets were chosen. Formulae used for the calculation of structural and optical

properties are given and explained. Some results from calculations of well studied semiconductors are presented to justify the choice of methodology.

Chapter 5 contains all results and analysis for GO and rGO. Results are discussed in detail and where appropriate, compared to experimental observations.

Chapter 6 summarises the most important results and findings and an evaluation of the outcomes of the study. Suggestions for future work and improvements are given, along with a critical appraisal of the methodology.

2

FUNCTIONALISATION OF GRAPHENE

BRIEF OVERVIEW OF THE PROPERTIES OF GRAPHENE

Structure

The most recent of carbon's allotropes to be discovered, the structure of graphene is equivalent to a single atomic layer of graphite. In a sense, 2D graphene can be viewed as the "building block" of many of the carbon allotropes, including 0D fullerenes, 1D nanotubes and 3D graphite. Figure 2.1.1 illustrates the real and reciprocal space structure of graphene, with the unit cell vectors, reciprocal lattice vectors and Brillouin zone points of high symmetry clearly indicated. The so-called "armchair" and "zigzag" directions are also illustrated.

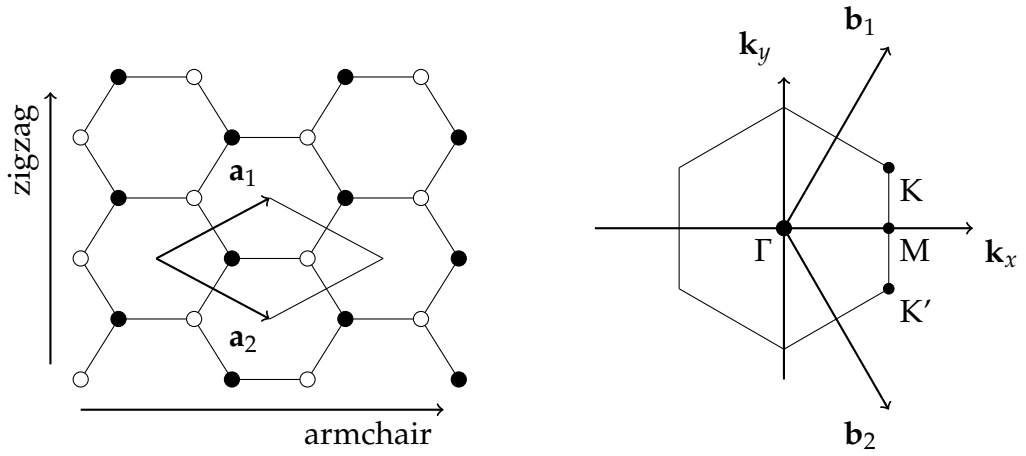

Figure 2.1.: Unit cell and first Brillouin zone of graphene. Unit cell vectors, reciprocal lattice vectors and armchair and zigzag directions are indicated.

The real and reciprocal lattice vectors are given as

$$\begin{aligned}
\mathbf{a}_1 &= \frac{\sqrt{3}a}{2}\hat{\mathbf{x}} + \frac{a}{2}\hat{\mathbf{y}}, \\
\mathbf{a}_2 &= \frac{\sqrt{3}a}{2}\hat{\mathbf{x}} - \frac{a}{2}\hat{\mathbf{y}}, \\
\mathbf{b}_1 &= \frac{2\pi}{\sqrt{3}a}\hat{\mathbf{x}} + \frac{2}{a}\hat{\mathbf{y}}, \\
\mathbf{b}_2 &= \frac{2\pi}{\sqrt{3}a}\hat{\mathbf{x}} - \frac{2}{a}\hat{\mathbf{y}},
\end{aligned} \tag{2.1}$$

where a is the lattice constant. For free graphene a = 2.461 Å and the carbon-carbon bond length is 1.418 Å. This latter quantity is in fact the average length of the single and double carbon bonds, which are described in detail in the following subsection, 2.1.2. As the neighbouring sites are not equivalent, the honeycomb structure is not a Bravais lattice. The structure can, however, be described by the hexagonal (trigonal) Bravais lattice with a basis of two atoms. The point group of the structure is D_{6h}, with 12 irreducible representations and 24 symmetry operations under which the geometry remains invariant.

Properties

Although only isolated by means of mechanical exfoliation in 2004 [1], graphene's electronic properties were studied theoretically as far back as 1947 [20]. Given that the interlayer spacing in graphite is considerably larger than the intralayer lattice parameter and therefore conduction takes place largely in-plane, its electronic structure was studied using a tight-binding model of a single atomic layer in order to obtain an approximation of graphite's band structure, or in other words, the band structure of graphene! It is also worth noting that the term graphene was first proposed in 1986 in the context of describing the intercalation of graphite [21].

Many superlatives are often used to describe graphene's mechanical, electronic and optical properties, with some justification. For example, it boasts an impressive and at the time of writing unparalleled, tensile strength of 130 GPa with an areal density of only 0.77 mgmm^{-2} [22]. The same study reported the Young's modulus as 1.0 TPa, while a a later measurement yielded 2.4 TPa [23], the latter of these values is approximately twice that of diamond. Graphene's elasticity is known to be highly non-linear, so the reporting of different values when tested under different amounts of strain is to be expected.

Of particular interest to this study are the electronic and optical properties. Of carbon's six electrons, four are available for bonding. In the graphene allotrope one of the 2s orbitals is excited to a 2p state, leaving a single 2s orbital and $2p_x$, $2p_y$ and $2p_z$ orbitals. The first three of these form a sp^2 hybridised orbital, characterised by three equally distributed planar lobes. This sp^2 orbital forms a σ bond with the sp^2 orbitals of the three nearest neighbouring carbon atoms. The symmetry of the sp^2 orbital results in

the distinctive hexagonal structure of graphene and graphite. It is also this network of σ bonds that is chiefly responsible for graphene's exceptional tensile strength. The remaining $2p_z$ orbital forms a π bond with one of its nearest neighbours. It is the highly delocalised electrons in the half-filled π band that are responsible for conduction and hence graphene's transport properties.

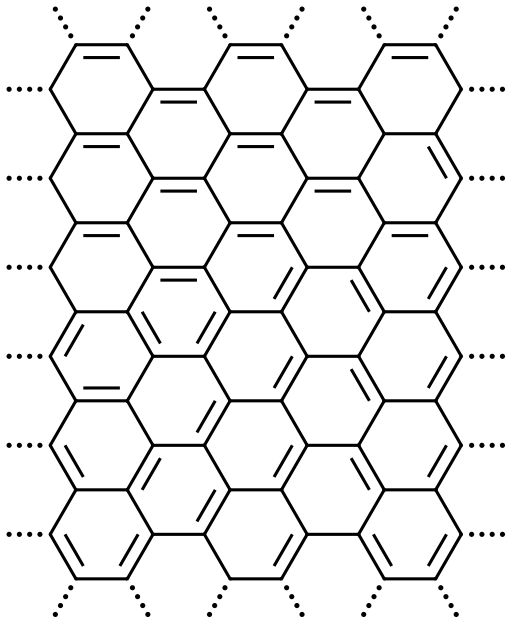

Figure 2.2.: Skeletal formula of graphene.

The electronic properties of graphene lie somewhere between those of a semiconductor and those of metal. Unlike a typical semiconductor, there is no band gap as the π and π^* bands meet at the K point of the IBZ [24]. Unlike a metal, however, the electron density of states is zero at the Fermi level. This leads to the description of graphene as either a zero band gap semiconductor or a semimetal. Another particularly distinguishing feature is that at the K point the dispersion relation of the conduction electrons in the π and π^* bands is effectively linear in the vicinity of the Fermi level, rather than parabolic as is typical of semiconductors and metals. These π

electrons behave in a relativistic manner and their behaviour is described by the Dirac equation, rather than the Schrödinger equation [3]. For this reason the electron quasiparticles are commonly referred to as massless Dirac fermions, or alternatively Graphinos. The associated points in the Brillouin zone are referred to as the Dirac points.

HYDROGENATED GRAPHENE

Much effort has been focused on modifying graphene's electronic structure in order to open a band gap. One successful method for achieving this is the hydrogenation of graphene. In the case of full hydrogen saturation, with a formula of $(C_1H_1)_n$, the resulting material is known as graphane. For levels of coverage below 100%, it is then known as partially hydrogenated graphene [25].

Interestingly, graphane was studied theoretically before graphene's discovery [26]. In fact, the successful synthesis of graphane as defined in the preceding paragraph has yet to be reported, only partial hydrogenation of graphene having thus far been achieved. Upon adsorption of hydrogen, the sp^2 hybridised bonds of graphene are rehybridised to sp^3, accompanied by an increase of the C-C bond length from 1.42 Å to 1.52-1.56 Å [27]. The rehybridisation also results in the disruption of the C-C π bonds. Graphane can exist in a number of stable conformational isomers with varying C-C bond lengths, hence the range. In all cases, the hexagonal symmetry is destroyed and the C-C bonds are not of uniform length, owing to the tetrahedral bond arrangement.

The disruption of the π band opens a finite band gap, reported at 3.5 eV or 3.7 eV, depending on the conformational isomer in question [27]. How-

ever, this study was carried out using density functional theory (DFT) with a generalised gradient approximation (GGA) density functional, which like all standard density functionals systematically underestimates band gaps.[1] The same study reports binding energies per atom of 6.53-6.56 eV, indicating very high structural stability.

At relatively high levels of coverage, ∼40%, adsorbed H atoms have been seen to form clusters, suggesting the possibility of controlling electronic properties by patterned adsorption [28, 29]. A combined experimental and theoretical study confirmed this possibility [30]. Angle-resolved photoemission spectroscopy (ARPES) measurements of graphene grown on an Ir(111) surface and then hydrogenated showed separation of the π and π^* bands to form a gap of 0.45 eV or greater. An increase of the π bandwidth was also observed.

OXIDISED GRAPHENE

Chemistry, structural and electronic properties

Modification of graphene's electronic structure can also be readily achieved by adsorption of atoms other than hydrogen, for example fluorine [31, 32], and oxygen [33, 34]. Oxidised graphene is commonly prepared via the oxidation of graphite, in which flake or powdered graphite is reacted with strong acids and oxidising agents to produce graphite oxide. This was originally achieved in the mid-nineteenth century by Brodie [35], although modern processes are typically based on the considerably less dangerous Hummers method [36–38]. The resulting graphite oxide is extremely hy-

1 See subsection 3.4.4 of chapter 3 for a detailed explanation of this.

drophilic and therefore easily dispersed in water [39]. The interplanar spacing increases linearly as a function of the oxidation level, allowing for the intercalation of water molecules [40]. Sheets of graphene oxide can subsequently be exfoliated by means of sonication of the colloidal suspension [41].

Production of graphene oxide via the Hummers method has attracted much consideration in recent years as an intermediate step in the quest for reliable, scalable and cheap production of high quality graphene [42–44]. However, chemical reduction of graphene oxide, in which aggressive reduction agents such as hydrazine or dimethylhydrazine are employed, has thus far proved unsuitable to this end [45–48]. Moreover, true monolayer graphene or rGO is very difficult to obtain using these methods [49]. This notwithstanding, graphene oxide boasts a range of important properties that mean it is of great interest to physicists, chemists, materials scientists, and engineers alike. [50–54]. In particular, studies of GO reveal some interesting optical properties that will be discussed in the following subsection [55].

Much effort has been placed on characterising the chemistry and structure of graphite oxide and GO, with considerable debate as to the actual definition of GO [56]. Chemical reduction of graphene oxide tends to produce a highly defective, amorphous material, on which epoxy and hydroxyl functional groups (see Figs. 2.3(a) and 2.3(b)) are formed on the basal plane, while carbonyl and carboxyl moieties (see Figs. 2.3(c) and 2.3(d)) are formed at the edges [57, 58]. This is accompanied by considerable deformation of the graphene sub-lattice and the formation of multiple point defects [59]. The binding energy of functional groups located at these de-

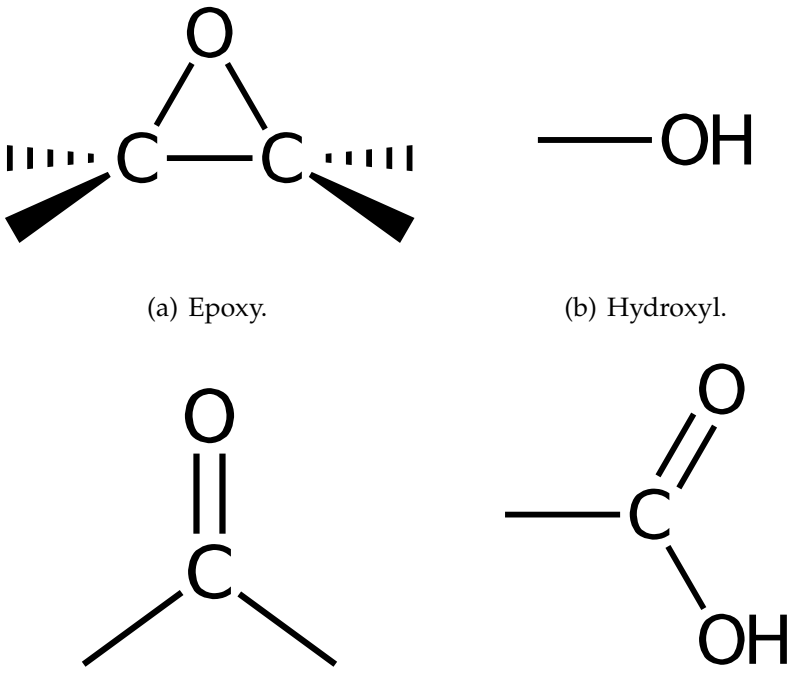

(a) Epoxy. (b) Hydroxyl.

(c) Carbonyl. (d) Carboxyl.

Figure 2.3.: Functional groups of oxidised graphene.

fect sites is increased, presenting a barrier to complete reduction of GO to graphene [60].

Several structural models for the layers of graphite oxide and hence GO, have been proposed [61]. The earliest of these, depicted in Fig. 2.4, dates to 1939 and suggests a model of purely epoxy functionalised graphite with alternating O coverage above and below atomic layers and a formula of C_2O [62]. This model turns out to be of direct relevance to this study, but does not faithfully represent graphite oxide produced by the methods discussed above.

A later model proposed to account for the presence of hydrogen posits a corrugated sp^3-bonded graphite layer populated with hydroxyl and 1,3-ether functional groups [63]. The sp^3 hybridisation and associated vertical displacement of the C atoms is a correct assumption, although the forma-

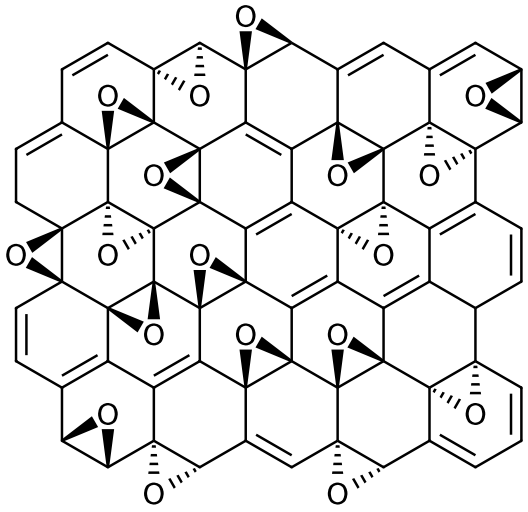

Figure 2.4.: Hofmann model of graphite oxide [62].

tion of 1,3-ether groups has been shown to be energetically unfavourable compared to that of epoxy (1,2-ether) moieties [64].

Three further models predict the corrugation of the graphite layers, with one comprising linked quinoidal chains [57, 65] and the other suggesting a graphite fluoride like structure, with layers linked by the O atoms in epoxy functional groups [66–68]. The most recently proposed model makes recourse to the structure of linked quinoidal chains with hydroxyl and 1,3-ether functional groups [61].

Arguably the most important model is that of Lerf and Klinowski, shown in Fig. 2.5. Based on extensive nuclear magnetic resonance (NMR) spectroscopy, this is the first model to account for all four dominant functional groups discussed above [69–72]. Again, both sides of the basal plane are covered with epoxy and hydroxyl moieties, while the edges are populated by carbonyl and carboxyl groups. Significantly, some sp^2 conjugated domains are predicted to remain intact.

Although the models discussed in the preceding paragraph represent useful models of the layers of graphite oxide and hence of GO, it is impor-

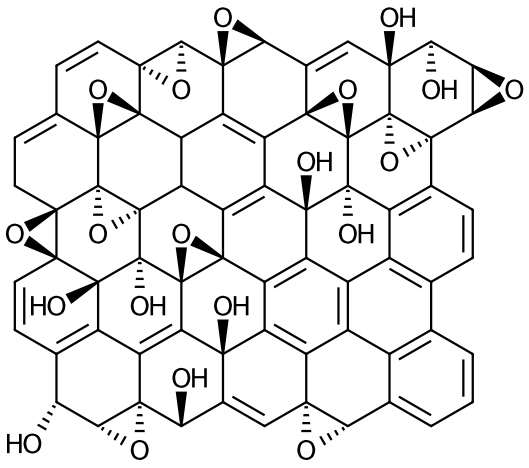

Figure 2.5.: Lerf-Klinowski model of graphite oxide, with carbonyl and carboxyl groups at edges omitted for clarity [69].

tant to note that the exact method of production, level of oxidation, and the precursor used strongly affect the structure and properties of the resulting material [56, 57]. For example, the exfoliation of GO by thermal expansion of graphite oxide is precipitated by the release of CO_2, the production of which reduces the C:O ratio from ∼2:1 to ∼10-20:1 [73, 74].

Subsequent experimental work confirms the presence of many of the features predicted in these models. Selected area electron diffraction (SAED) measurements of graphite oxide prepared by a modified Brodie method confirm that it retains a graphite-like structure, while NMR spectroscopy of the same material reveals peaks associated with sp^2 hybridised C atoms, as well as hydroxyl and epoxy functional groups [75]. Carbonyl and alkyl groups are also in evidence. X-ray absorption spectroscopy (XAS) reveals the availability of unoccupied π^* and σ^* states, attributable to sp^2 hybridised carbon atoms [76]. Fourier transform infrared (FTIR) spectroscopy confirms the Lerf-Klinowski model with epoxy and hydroxyl groups observed on the basal plane and carboxyl and alkyl groups at the edges.

Atomic force microscopy (AFM) measurements of hydrazine reduced GO show the material to be rough, with the average roughness of the surface reported as $\sim$6 Å [77]. The authors of this study attribute this to the corrugation of the graphene sub-lattice. Annular dark field imaging (ADF) and electron energy loss spectroscopy (EELS) performed in the same study found that $\sim$40% of bonds were sp^3 hybridised, with a C:O ratio of 5:1. DFT calculations carried out to support the study confirmed that the formation of sp^3 bonds cause the vertical displacement of C atoms and is thus responsible for the corrugation observed.

Near-edge X-ray absorption fine-structure spectroscopy (NEXAFS) and transmission-electron microscopy (TEM) studies of free-standing GO membranes produced by the Hummers method again show epoxy, hydroxyl, carbonyl and carboxyl moieties to be present [78]. In contrast to many other studies but in line with Ref. [61], however, it is suggested that some carbonyl groups are bonded to aromatic rings on the basal plane. Also counter to other experimental observations, the GO displays a degree of order, with alternating nm-scale regions of sp^2 conjugated graphene and O functionalised domains. The functionalised domains also do not exhibit the high concentration of defects previously seen [58]. Although this suggests that Hummers GO may be suitable for use in photonic and micro/nano-electronic devices after all, the thickness of the membranes unfortunately varies from a single layer to approximately 10 layers.

An alternative approach to the harsh chemistry of such "top-down" methods for the production of GO is the oxidation of graphene by exposure to atomic oxygen [79], molecular oxygen at high temperature [80], or water-vapour plasma [81]. Such methods promise a much greater level of control over the resulting material.

The use of atomic rather than molecular oxygen is preferable owing to the fact that the latter is not reactive enough at room temperature to disassociate and chemisorb to the aromatic rings. An NEXAFS and X-ray photoelectron spectroscopy (XPS) study of O adsorption on epitaxial graphene grown on both Ir(111) and Pt(111) surfaces, to which it is only weakly adsorbed, shows the O atoms to adsorb at bridge sites to form epoxy functional groups [82]. Again, there is no evidence of the formation of 1,3-ether groups. As observed in GO produced by wet chemical synthesis, the ensuing change from sp^2 to sp^3 bonding in the functionalised and neighbouring C atoms causes buckling of the graphene. The lattice mismatch between the substrate and graphene leads to the formation of a Moiré pattern, with some areas accordingly more strongly coupled. The lattice buckling is more pronounced in such areas, as the disruption of the C-C π bonds results in the nearest neighbouring C atoms to the functional groups to bond more strongly to the substrate. A greater concentration of adsorbates is also observed at these sites. The oxidation process is not entirely reversible as, upon annealing, vacancy defects are formed by oxygen etching in the weakly coupled domains.

A fully reversible process has been demonstrated in which graphene grown epitaxially on a SiC(0001) surface is functionalised by atomic oxygen under ultrahigh vacuum (UHV) [83]. As with the previous study, the chemisorption of O in this "bottom-up" technique forms only epoxy functional groups, and causes no damage to the underlying honeycomb lattice. In contrast to earlier efforts, the process was shown to be reversible both under annealing and by desorption with a negatively-biased scanning tunnelling microscope (STM) tip. This is likely due to the fact that interaction with the substrate is much stronger than in the case of graphene grown on

transition metal surfaces, with $\sim 1/3$ of the C atoms involved in covalent bonding with the terminating Si atoms [84]. The barrier to defect formation can be expected to be much higher in this case, reducing the likelihood of oxidative etching. This leads to the prospect of producing GO with highly tunable properties.

Most recently, a method for producing patterned graphene and GO using femtosecond laser induced two-photon oxidation has been demonstrated [85]. Such a method could allow for the production of GO with a very precise degree of control over the energy gap and optical properties.

Ab initio DFT calculations have been performed by numerous groups in order to gain further insight into the processes and effects of the oxidation of graphite and graphene, and to aid in the interpretation of experimental observations. Estimates of the energy gap and its relationship to the level of oxidation, type of functionalisation, and structure are also obtained from these calculations. One early study examined the model of mixed phase epoxy and hydroxyl functionalised graphene proposed in Ref. [67], with formulae of the phases being C_8O_2 and $C_8(OH)_4$ respectively [86]. This structure was found to be most stable with 75% of the graphene surface functionalised (i.e. 75% of the C atoms directly bonded to adsorbates), with a suggested formula of $C_8(OH)_4O$. Upon decreasing to 25% O coverage the material undergoes transition to a conducting phase. Energy gaps for the semiconducting phase are reported to be in the range 1.8-2.8 eV, although this is based on local density approximation (LDA) calculations meaning that the physical value should be somewhat higher.

A more recent work disputes this result regarding the stability of GO [87]. This study, carried out at the generalised gradient approximation level of theory, predicts GO to be most thermodynamically stable at 100% surface

functionalisation, in which all C-C bonds sp^3 hybridised. The results were found to hold true whether the structure is a single phase of either epoxy or hydroxyl functionalised graphene, or a mixture of both phases. The authors suggest that GO containing regions of sp^2 bonded carbon exists as a meta-stable phase favoured by reaction kinetics and caused by the lattice mismatch between these regions and the functionalised regions.

Further DFT studies have been published that investigate the properties of ideal periodic GO structures, both epoxy and hydroxyl functionalised. One carried out at the local density approximation level of theory reports energy gaps in the range 0-4 eV, depending on the coverage and type of functionalisation [88]. Of particular interest is one configuration of fully oxidised graphene presented with unit formula C_2O, where epoxy groups are formed at bridge sites alternating above and below the graphene lattice along the armchair direction.

Such alternating O coverage is reported to be energetically favourable as it minimises the buckling associated with the bond reconfiguration [89]. A combination of DFT and *ab initio* molecular dynamics calculations show stability to increase with increasing O coverage, although in an oscillating manner. The binding energy per O atom is given as 3.34 eV for two sided coverage of 0.5 ML and 2.80 eV for single sided, with adsorption at bridge sites along the armchair direction. The energy gap of the latter is given as 3.25 eV, but this can again only be considered qualitatively due to the GGA functional used in the calculation.

A GGA study of the evolution of the energy gap of reduced epoxy-functionalised graphene oxide with respect to O coverage reveals that the relationship is not monotonic [90]. This particular study considers structures with relatively homogeneous O coverage on one side of the graphene

lattice only and predicts a quadratic relationship between the level of O coverage and the relaxed lattice constant. The most thermodynamically stable predicted structures are all of low but varying symmetry, either of point group C_1, C_s, C_2, or C_{2v}. This points to the importance of symmetry in controlling the gap, which has been well studied and exploited in graphene [91–93]. The calculated gaps reported range from 0.109 eV at 6.25% coverage ($C_{64}O_4$) to 3.004 eV at 50% coverage (C_4O_2).

The formation of a sizeable gap has been reported even for low levels of O coverage [94]. Again using a GGA functional, a gap of 1.19 eV was calculated for $(C_{16}O)_n$ and 1.58 eV for $(C_{32}O_3)_n$. The authors explicitly acknowledge the limitations of the approximation, but assert that the predicted trends are accurate.

One work of particular importance to this study, as it forms the starting point, investigates the adsorption of O atoms in clusters of increasing size [95]. The O binding energy was found to increase monotonically with respect to increasing O coverage. A number of configurations of fully oxidised graphene were considered, confirming previous findings that alternating coverage above and below the graphene sub-lattice at 0.5 ML is the most stable arrangement. Adsorption at bridge sites along the zigzag direction was also noted to result in greater stability than adsorption at equivalent sites along the armchair direction, with binding energy per O atom reported at 3.25 eV and 3.23 eV respectively. The GGA calculated band gap for the most stable structure was given as 4.8 eV.

Optical properties

It is evident that substantial control of the energy gap can be achieved by varying the level of oxidation of graphene. Experimental evidence from UV-visible (UV-vis) and photoluminescence (PL) spectroscopy indicates that the optical properties of GO follow these trends. Strong photon absorption in the ultraviolet (UV) range has been observed in aqueous solutions of graphite oxide and GO [96]. Reduction of GO by exposure to hydrazine is reported to red-shift the UV absorption peaks as a function of exposure time, owing to the partial restoration of the sp^2 associated π bonds [7].

Nanometre-scale flakes of PEGylated [1] graphene oxide, investigated for potential applications to drug delivery and cellular imaging, display photoluminescence (PL) emission in the visible and infrared (IR) ranges, in addition to strong optical absorption [97]. Despite the diameter of flakes studied ranging between $\sim$10 nm and 300 nm, the PL and absorption spectra were found to be almost identical between samples. This is in contrast to the expected result that quantum confinement effects caused by the flake diameter would strongly affect the optical properties. The authors propose that small sp^2 conjugated domains, of diameter $\sim$1 nm to 5 nm, within the flake are the origin of the PL effects. A further study of the same system reports similar findings, as well as fluorescence in the UV and visible ranges [98].

PL is also observed in solid GO produced from suspension by the drop casting method [99]. Similarly to the observations from UV-vis spectra, the PL peaks are red-shifted as the level of oxidation is reduced. The PL peaks are rather broad and a heterogeneous electronic structure with a disper-

1 PEGylation refers to the attachment of chains of polyethylene glycol to molecules in order to improve drug delivery.

sion of energy gaps is postulated. It is also suggested that nonradiative relaxation processes are present.

Blue and near-UV photoemission was observed in high quality "thoroughly exfoliated" suspensions of GO [100]. The previous reports of visible and near-IR PL emission were also verified, but from samples retrieved from "poorly dispersed suspensions". As with these studies, the PL effects are attributed to small sp^2 domains within the sp^3 bonded GO flakes and films. The gap between the highly localised π and π^* states associated with the sp^2 domains is explained to lie within the σ-σ^* gap of the wider structure. Controlling the size of these domains is suggested as a mechanism for tuning the π-π^* gap and thus the optical properties of GO for optoelectronics applications.

Spectroscopic ellipsometry (SE) was performed on thin films of GO at various levels of reduction in order to, in conjunction with analysis of results using the Lorentz oscillator method, more accurately characterise the optical properties [101]. The authors conclude that the optical response of few layer reduced GO is very similar to that of graphene in the visible range, suggesting it as a possible substitution for the latter. However, the Lorentz oscillator model used in this study was parameterised using the theoretically predicted band gaps discussed in the preceding subsection, which are beyond doubt too small. [102]

UV-vis spectroscopy has been used to measure the optical gap during hydrazine reduction of GO synthesised by a modified Hummers method [103]. The gap of the starting material with a C:O ratio of $\sim$ 1.7:1 was measured as 3.5 eV, which decreased to 1.0 eV as the C:O ratio was reduced to $\sim$ 4.5:1. The optical gap was not observed to dip below this value, due to residual O functional groups and the presence of structural defects.

Quantum confinement induced excitons in sp^2 domains within GO were studied using X-ray absorption near edge structure spectroscopy (XANES) [104]. The presence of excitons is essential for optoelectronic devices. In conjunction with DFT simulations at the LDA level of theory and quasi-particle corrections via the GW method, this study shows the presence of excitons localised within the sp^2 regions, which are postulated to give rise to the PL observed in GO. The PL decay times are reported to be proportional to the size of the graphene domain, akin to the behaviour of quantum dots [53].

A study of graphene quantum dots (GQDs) and GO quantum dots (GOQDs) elucidates on this latter finding [105]. The peak PL intensity is observed to be stronger in the GQDs than the GOQDs, with the former emitting blue photons and the latter emitting green. The relative red-shift is attributed to O states. The GOQDs are observed to possess more favourable radiative recombination dynamics, with slower decay rates at all excitation wavelengths evident from time-resolved photoluminescence spectroscopy (TRPL). This property is of great importance to photovoltaics (PV) applications.

The effects of the presence of O states on optical properties has been exploited to synthesise GOQDs and reduced graphene oxide quantum dots (rGOQD) with tunable PL [106]. GOQDs were fabricated by the oxidation of GQDs using a modified Hummers method, which were in turn reduced in acid to produce rGOQDs. The mechanism for luminescence in GOQDs is ascribed to the clusters of O functional groups formed on the basal plane. Conversely, for rGOQDs the PL originates from small sp^2 domains embedded in the wider sp^3 bonding matrix, in agreement with earlier findings [100].

PL spectroscopy has been used to probe the band structure of GO in aqueous suspension at different levels of reduction in ascorbic acid [107]. Three of four peaks in the PL and photoluminescence excitation (PLE) spectra were identified to be associated with GO, the two highest in energy corresponding to peaks in the UV-vis spectrum and the third as a long absorption tail. The first appears at 4.05 eV in the PL spectrum, 6.20 eV in the PLE spectrum, and 6.53 eV in the UV-vis spectrum. This is attributed to the σ-σ^* transition. The second peak at 3.44 eV, 5.39 eV, and 5.39 eV in the PL, PLE, and UV-vis spectra respectively, is attributed to the π-π^* transition and is seen to red-shift upon reduction. This is once again in good agreement with earlier experimental observations [100]. A broad peak appearing from 3.31 eV to 2.82 eV in the PL spectrum and corresponding respectively to a peak in the PLE and long absorption tail in the UV-vis spectra at 4.20 eV. This is ascribed to π states localised on O atoms. The energy gap is calculated from the slope of the UV-vis spectrum to be 3.50 eV, again in agreement with earlier work [103, 108]. This falls closely in line with the π-π^* peak in the PL spectrum.

Photonics device applications

As alluded to in the introduction, the applications of GO and rGO are manifold. However, given the most interesting and importantly controllable optical properties of these materials, photonic device applications are of particular interest [109].

One particularly promising use for rGO is as a transparent electrode in heterojunction PV devices [110]. Indium tin oxide (ITO) is commonly used for this purpose, but owing to the scarcity of Indium, cost of production,

and some unfavourable characteristics, a replacement material is highly sought after [111]. An additional advantage over ITO, which is brittle, is that rGO films are highly flexible [112].

In spite of the aforementioned problems with graphene, GO, and rGO produced by wet synthesis, it is of great interest to the manufacture of PV devices as solution-process methods offer a much cheaper alternative to deposition and epitaxial growth methods. Spin coating of dispersed GO prior followed by reduction has been investigated as a means of producing transparent electrodes for organic PV cells [113, 114]. The device performance is unfortunately poor, mostly as a result of the high sheet resistance of the electrodes. Greatly improved performance has been achieved using photothermally reduced GO and rGO mesh electrodes [115, 116].

GO also shows great promise as an efficient hole transport layer in polymer PV cells [117]. Recombination lifetimes of 11.6 μs were measured, demonstrating good carrier separation and hole transport [118, 119]. This has been used to produce organic PV cells of substantially increased area and efficiency [120]. Performance has been further increased by using GO nanoribbons instead of GO films [121].

In addition to hole transport, considerable device performance improvements have also been realised by using rGO/metal oxide composite electron transport layers over metal-oxides alone [122].

Inverted polymer solar cells with an efficiency of 4.15% have been produced using an rGO and zinc oxide (ZnO) composite n-type buffer layer [123]. The use of composite rGO-ZnO afforded an improvement in the short-circuit current (J_{sc}) of 36% over devices using ZnO alone. This is reported to be due to more favourable recombination dynamics.

3

DENSITY FUNCTIONAL THEORY

SIMPLIFYING THE MANY ELECTRON PROBLEM

Schrödinger's wave formulation and Heisenberg's equivalent matrix formulation of quantum mechanics allow exact solutions for only the simplest of physical systems. Indeed, even the helium atom may only be treated approximately. The first challenge is the sheer scale of the problem, which exists in a space of dimension $3N+1$, where N is the number of particles. This is exacerbated by the electron-electron and electron-nuclei Coulomb interactions, the inclusion of which leads to a system of $3N+1$ coupled differential equations. It is immediately apparent that an exact solution for heavier atoms, molecules and solids is not possible.

In order to deal with these many electron problems, it is therefore necessary to make a number of approximations. The first of these to be applied is typically the Born-Oppenheimer, or adiabatic, approximation. This assumes that electrons respond instantaneously, or adiabatically, to changes in the position of the nuclei, while the reverse does not hold true. The nuclei can then effectively be treated as classical point-like particles. This essentially halves the size of the problem space. The validity of this as-

sumption relies on the substantial difference in mass, several orders of magnitude, between nuclei and electrons. The nuclei are therefore considered to be of infinite mass and the many-electron Hamiltonian is thus

$$H = \underbrace{-\sum_i \frac{\hbar^2}{2m}\nabla^2_{\mathbf{r}_i}}_{T} \underbrace{-\sum_i \sum_I \frac{Z_I e^2}{4\pi\varepsilon_0 |\mathbf{R}_I - \mathbf{r}_i|}}_{V_{\text{ext}}} + \underbrace{\frac{1}{2}\sum_i \sum_{j\neq i} \frac{e^2}{4\pi\varepsilon_0 |\mathbf{r}_i - \mathbf{r}_j|}}_{V_{\text{ee}}}, \tag{3.1}$$

where $\hbar$ is the reduced Planck's constant, m is the electron rest mass, $\mathbf{r}_i$ and $\mathbf{R}_I$ are the electron and ion positions, respectively, and Z_I is the atomic number of the I^{th} ion. The electron-ion potential is typically known as the external potential as the ions are being treated as classical objects and are thus *external* to the system. Notwithstanding the still possibly boundless size of the system, the third term of the Hamiltonian, which describes the electron-electron interaction, presents an intractable problem. To effect further simplification, it is evident that some approximation of this interaction is required.

Much of this chapter follows Kaxiras' "Atomic and Electronic Structure of Solids" [124], while reference is also made to Martin's "Electronic Structure" [125] and Parr and Yang's "Density-Functional Theory of Atoms and Molecules" [126].

SINGLE PARTICLE APPROXIMATIONS AND THE VARIATIONAL METHOD

The one electron, or independent electron, approximation is an approach that forms the basis many of the most commonly used computational condensed matter physics and quantum chemistry methods. The simplest

form of the many body wavefunction is composed of a linear product of N one-electron orbitals, such that $\Psi(\{\mathbf{r}\}) = \prod_{i=1}^{N} \phi_i(\mathbf{r}_i)$. This is called the Hartree product. All electrons are treated independently and in a simple approximation to V_{ee} interact only through a mean field potential, the Hartree Potential, resulting from the charge density of the remaining $N-1$ electrons:

$$V_{\text{H}}(\mathbf{r}) = e^2 \int \frac{\rho(\mathbf{r}')}{|\mathbf{r} - \mathbf{r}'|} \mathrm{d}\mathbf{r}'. \tag{3.2}$$

That the potential felt by each electron is unique is made more obvious by representing the Hartree potential in terms of the one electron orbitals, such that

$$V_{\text{H}}^{(i)}(\mathbf{r}) = e^2 \sum_{j \neq i} \int \frac{|\phi_j(\mathbf{r}_j)|^2}{|\mathbf{r}_i - \mathbf{r}_j|} \mathrm{d}\mathbf{r}_j. \tag{3.3}$$

Reintroducing the kinetic energy and external potential terms to complete the Hamiltonian, the total energy is then given by

$$\begin{aligned} E &= \langle \Psi | \, H \, | \Psi \rangle \\ &= -\frac{1}{2} \sum_{i}^{N} \int \phi_i^* \nabla_i^2 \phi_i \mathrm{d}\mathbf{r} - \sum_{i}^{N} \int \phi_i^* V_{\text{ext}} \, \phi_i \mathrm{d}\mathbf{r} \\ &+ \frac{1}{2} \sum_{i \neq j}^{N} \int \frac{\phi_i^*(\mathbf{r}_1) \phi_i(\mathbf{r}_1) \phi_j^*(\mathbf{r}_2) \phi_j(\mathbf{r}_2)}{|\mathbf{r}_i - \mathbf{r}_j|} \mathrm{d}\mathbf{r}_1 \mathrm{d}\mathbf{r}_2. \end{aligned} \tag{3.4}$$

For convenience Hartree atomic units, in which $e = \hbar = m_e = 4\pi\varepsilon_0 = 1$, have been adopted and will be used all but exclusively from this point forth, unless explicitly stated otherwise.

To solve and find the wavefunction, the Lagrangian method of constrained optimisation is used. The Lagrangian of the system is given by

$$\mathcal{L}[\{\phi_i\}] = \langle \Psi | \, H \, | \Psi \rangle - \left[\sum_{i=1}^{N} \varepsilon_i \langle \phi_i | \, \phi_i \rangle - \delta_{ij} \right], \tag{3.5}$$

where ε_i are Lagrange multipliers enforcing the constraint that the one electron orbitals remain orthonormal, i.e. $\langle \phi_i | \, \phi_i \rangle = \delta_{ij}$. The functional derivative of the Lagrangian with respect to $\langle \phi_m |$, where $m = 1, 2, \ldots N$, is now set equal to zero, such that

$$\frac{\delta \mathcal{L}[\{\phi_i\}]}{\delta \langle \phi_m |} = 0. \tag{3.6}$$

Varying the one electron orbitals, an N-electron system then results in a system of N single particle Schrödinger equations, known as the Hartree equations,

$$\left[-\frac{1}{2} \nabla_i^2 + V_{\text{ext}}(\mathbf{r}) + V_{\text{H}}^{(i)}(\mathbf{r}) \right] \phi_i(\mathbf{r}) = \varepsilon_i \phi_i(\mathbf{r}), \tag{3.7}$$

where the Lagrange multipliers ε_i are the energy eigenvalues of these orbitals. This method is known as the Rayleigh-Ritz variational principle.

The Hartree equations may be solved self-consistently for the complete set of orbitals and thus the mean field wavefunction. However, in addition to being a rather crude approximation to the electron-electron interaction, the Hartree method neglects the fermionic nature of electrons and is inadequate for the prediction of properties of real systems.

THE HARTREE FOCK APPROXIMATION

The oldest of the approximations to the many-electron interacting system still in widespread use in quantum chemistry is the Hartree-Fock method, often known as the self-consistent field (SCF) method. A brief overview of this method is in order as its formalism is of importance to the hybrid density functionals discussed later in section 3.5. This approximation is closely related to the earlier Hartree approximation, but affords a considerable improvement over it by correctly treating electrons as fermions, that is to say that the anti-symmetry of the wavefunction with respect to exchange is observed. The N electron wavefunction is formed by a Slater determinant [127] of one electron orbitals,

$$\Psi(\{\mathbf{r}_i\}) = \frac{1}{\sqrt{N!}} \begin{vmatrix} \phi_1(\mathbf{r}_1) & \phi_1(\mathbf{r}_2) & \cdots & \phi_1(\mathbf{r}_N) \\ \phi_2(\mathbf{r}_1) & \phi_2(\mathbf{r}_2) & \cdots & \phi_2(\mathbf{r}_N) \\ \vdots & \vdots & \ddots & \vdots \\ \phi_N(\mathbf{r}_1) & \phi_N(\mathbf{r}_2) & \cdots & \phi_N(\mathbf{r}_N) \end{vmatrix}. \tag{3.8}$$

It is immediately clear that $\Psi(r_1, r_2, \cdots, r_N) = -\Psi(r_2, r_1, \cdots, r_N)$, as required. The total energy includes an additional term over that of the Hartree approximation, the exchange energy, which relates to the determinental form of the wavefunction and is given by

$$
\begin{aligned}
E = &-\frac{1}{2}\sum_{i}^{N}\int \phi_i^*\nabla_i^2\phi_i \mathrm{d}\mathbf{r} - \sum_{i}^{N}\int \phi_i^* V_{\text{ext}}\,\phi_i \mathrm{d}\mathbf{r} \\
&+\frac{1}{2}\sum_{i,j}^{N}\int \frac{\phi_i^*(\mathbf{r}_1)\phi_i(\mathbf{r}_1)\phi_j^*(\mathbf{r}_2)\phi_j(\mathbf{r}_2)}{|\mathbf{r}_i-\mathbf{r}_j|}\mathrm{d}\mathbf{r}_1\mathrm{d}\mathbf{r}_2 \\
&-\frac{1}{2}\sum_{i,j}^{N}\int \frac{\phi_i^*(\mathbf{r}_1)\phi_j(\mathbf{r}_1)\phi_i^*(\mathbf{r}_2)\phi_j(\mathbf{r}_2)}{|\mathbf{r}_i-\mathbf{r}_j|}\mathrm{d}\mathbf{r}_1\mathrm{d}\mathbf{r}_2. \qquad (3.9)
\end{aligned}
$$

The exchange energy arises from the "swapping" of indices of two electrons, causing electrons of the same spin to repel each other in accordance with the Pauli exclusion principle. Crucially, this term cancels out the non-physical self-interaction in the Coulomb potential when $j = i$.

The variational principle is again invoked. Upon variation of the Lagrangian of the same form as eq. 3.6 with respect to the orbitals in exactly the same manner as for the Hartree approximation, the Hartree-Fock equations are reached:

$$
\left[-\frac{1}{2}\nabla_i^2 + V_{\text{ext}}(\mathbf{r}) + V_{\text{H}}^{(i)}(\mathbf{r}) + V_{\text{x}}^{(i)}(\mathbf{r})\right]\phi_i(\mathbf{r}) = \varepsilon_i\phi_i(\mathbf{r}), \qquad (3.10)
$$

where $V_{\text{x}}^{(i)}$ is the exchange potential.

The Hartree-Fock equations may be solved exactly in real space, but are typically solved by expansion in a basis set of trial orbitals, in which case they are known as the Hartree-Fock-Roothaan equations [128]. This method has been used extensively in the quantum chemistry community for many decades. The explicit inclusion of the non-local electron exchange interaction is particularly useful, however the neglect of electron correlation effects limits the method's utility to solid state physics, where it seriously overestimates the energy gaps and fails completely for metals.

The effect of correlation is commonly dealt with using post-SCF techniques, including second (or higher) order Møller-Plesset perturbation theory (MP2) or multi-determinant methods such as the configuration interaction (CI). The computational expense and unfavourable scaling presently limit these to molecules consisting of tens of atoms. The dependency on the Hartree-Fock wavefunction again limits their usefulness to solid state physics.

DENSITY FUNCTIONAL THEORY

Origins and the Hohenberg Kohn Theorems

Although the origins of DFT can be traced back to some of the pioneers of quantum mechanics, Thomas [129], Fermi [130] and later Dirac [131], the basis of the modern theory is to be found in the theorems of Hohenberg and Kohn [132]. Common to these models is the replacement of the intractably complicated many-electron wavefunction, $\Psi(\mathbf{r}_1, \mathbf{r}_2, ..., \mathbf{r}_N)$, with the electron density, $\rho(\mathbf{r})$, thereby drastically reducing the number of dimensions of the problem.

The first Hohenberg-Kohn theorem states that the ground state charge density of a given system, $\rho_0(\mathbf{r})$, uniquely determines the external potential of that system, i.e. the species and positions of all atoms, up to a "trivial additive constant". In other words, the mapping $v_{\text{ext}}(\mathbf{r}) \mapsto \rho_0(\mathbf{r})$ is *invertible*. Conversely it might be said that no two different external potentials can produce the same charge density.

This statement is easily proved by contradiction. Assume that $\rho_0(\mathbf{r})$ may indeed be produced by two external potentials $v^{(1)}_{\text{ext}}(\mathbf{r})$ and $v^{(2)}_{\text{ext}}(\mathbf{r})$ differing

by more than a trivial additive constant c, such that $v_{\text{ext}}^{(1)}(\mathbf{r}) \neq v_{\text{ext}}^{(2)}(\mathbf{r}) + c$. Further assume that the ground state wavefunctions corresponding to the two potentials, $\Psi_1(\mathbf{r})$ and $\Psi_2(\mathbf{r})$, are non-degenerate, i.e. $E_1 \neq E_2$. Using the variational principle leads to the inequality

$$\begin{aligned} E_1 &< \langle \Psi_2(\mathbf{r}) | \, H_1 \, | \Psi_2(\mathbf{r}) \rangle \\ &= \langle \Psi_2(\mathbf{r}) | \, H_2 \, | \Psi_2(\mathbf{r}) \rangle + \langle \Psi_2(\mathbf{r}) | \, H_1 - H_2 \, | \Psi_2(\mathbf{r}) \rangle \\ &= E_2 + \int \left[v_{\text{ext}}^{(1)}(\mathbf{r}) - v_{\text{ext}}^{(2)}(\mathbf{r}) \right] \rho_0(\mathbf{r}) \mathrm{d}\mathbf{r}. \end{aligned} \tag{3.11}$$

Changing labels gives

$$E_2 < E_1 + \int \left[v_{\text{ext}}^{(2)}(\mathbf{r}) - v_{\text{ext}}^{(1)}(\mathbf{r}) \right] \rho_0(\mathbf{r}) \mathrm{d}\mathbf{r}. \tag{3.12}$$

Combining these two expressions leaves the absurd inequality $E_1 + E_2 < E_2 + E_1$, thereby proving the first Hohenberg-Kohn theorem. This implies a direct one-to-one mapping between the ground state charge density and the wavefunction and hence all system properties, *including* those of excited states.

The second Hohenberg-Kohn theorem states that the total energy is defined by a *universal* functional of the density and establishes a variational principle. The density that globally minimises this functional, giving the ground state energy, is the *exact* ground state density. The functional is defined as

$$E_{\mathrm{HK}}[\rho(\mathbf{r})] = T[\rho(\mathbf{r})] + V_{\mathrm{ee}}[\rho(\mathbf{r})] + \int v_{\mathrm{ext}}\,\rho(\mathbf{r})\mathrm{d}\mathbf{r},$$
$$= F_{\mathrm{HK}}[\rho(\mathbf{r})] + \int v_{\mathrm{ext}}\,\rho(\mathbf{r})\mathrm{d}\mathbf{r}, \tag{3.13}$$

where $F_{\mathrm{HK}}[\rho(\mathbf{r})]$ is the universal functional, encapsulating kinetic and electron-electron interaction contributions to the total energy. This theorem is simply proved by again making recourse to the Rayleigh-Ritz variational principle. Having already established that no two non-trivially differing ground state charge densities can produce the same external potential and hence ground state wavefunction, it follows that

$$E[\rho_1(\mathbf{r})] = \left\langle \Psi_1 \right| H_{\mathrm{HK}}^{(0)} \left| \Psi_1 \right\rangle > \left\langle \Psi_0 \right| H_{\mathrm{HK}}^{(0)} \left| \Psi_0 \right\rangle = E_0, \tag{3.14}$$

where ρ_0 and Ψ_0 are the ground state density and corresponding wavefunction mapped by the Hamiltonian $H_{\mathrm{HK}}^{(0)}$, and ρ_1 and Ψ_1 are an arbitrary density and corresponding wavefunction.

Unfortunately the form of the universal functional remains unknown and in practise the solution is as out of reach as that of the many body Schrödinger equation. Approximations can be made to the functional, but as this applies to both kinetic and electron-electron interactions, these are typically unsatisfactory and therefore not in wide use.

Kohn-Sham DFT

The problem was recast by Kohn and Sham to replace the many electron interacting system with a non-interacting auxiliary system [133]. The den-

sity is determined by one electron orbitals, $\phi_i(\mathbf{r})$, known as the Kohn-Sham orbitals:

$$\rho(\mathbf{r}) = \sum_i |\phi_{KS}^{(i)}(\mathbf{r})|^2. \tag{3.15}$$

It is important to note that these are the orbitals of a fictitious non-interacting system and cannot be interpreted with the same physical meaning as in the Hartree and Hartree-Fock approximations. A Slater determinant of the N occupied Kohn-Sham orbitals would describe the wavefunction of this auxiliary system.

The total energy is a still a functional of the density, but the functional is split into multiple parts such that

$$\begin{aligned} E[\rho(\mathbf{r})] = &-\frac{1}{2}\sum_{i=1}^{N}\int \phi_i^*(\mathbf{r})\nabla^2\phi_i(\mathbf{r})\mathrm{d}\mathbf{r} + \int \rho(\mathbf{r})V_{\text{ext}}\mathrm{d}\mathbf{r} \\ &+ \int\int \frac{\rho(\mathbf{r})\rho(\mathbf{r}')}{|\mathbf{r}-\mathbf{r}'|}\mathrm{d}\mathbf{r}\mathrm{d}\mathbf{r}' + E_{\text{xc}}[\rho(\mathbf{r})], \end{aligned} \tag{3.16}$$

where E_{xc} is the exchange-correlation functional,[1] which connects the true interacting and fictitious auxiliary systems. The form of this universal functional is again unknown, however, approximations can be made that are accurate for many systems.

The simplest approximation to the exchange-correlation potential and that presented in the original paper, is known as the local density approximation (LDA). The exchange-correlation potential is given by the func-

1 The term exchange-correlation functional can be misleading, as neither effect is treated explicitly: Rather the functional exists to correct for their absence.

tional derivative of the exchange-correlation functional with respect to the density:

$$V_{\mathrm{xc}}(\mathbf{r}) = \frac{\delta E_{\mathrm{xc}}}{\delta \rho(\mathbf{r})}. \tag{3.17}$$

The effective potential of the auxiliary system is

$$V_{\mathrm{eff}} = V_{\mathrm{ext}}(\mathbf{r}) + V_{\mathrm{H}}(\mathbf{r}) + V_{\mathrm{xc}}(\mathbf{r}). \tag{3.18}$$

The Kohn-Sham orbitals are solutions of one electron Schrödinger-like equations of similar form to Eq. 3.7, known as the Kohn-Sham equations:

$$\left[-\frac{1}{2}\nabla_i^2 + V_{\mathrm{eff}}^{(i)}(\mathbf{r})\right] \phi_i(\mathbf{r}) = \varepsilon_i \phi_i(\mathbf{r}), \tag{3.19}$$

The equations are solved self-consistently following the algorithm shown in Fig. 3.1. Self-consistency is achieved when the difference between the input and output densities is less than or equal to some predefined tolerance, corresponding to the global minimum of the potential.

Despite the expectation of Kohn and Sham that the LDA would not accurately predict chemical bonding, the results for ionic, covalent and metallic bonded systems tend to be remarkably accurate [134]. However, in the intervening years several approximations and numerous functionals based upon them have been developed, each with the aim of improving the prediction of particular properties or to make possible the study of difficult systems [135].

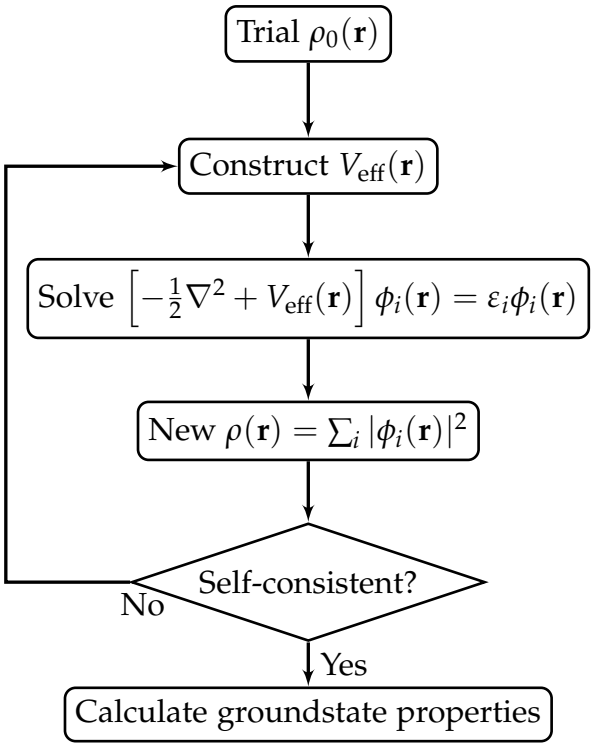

Figure 3.1.: Self-consistent solution of the Kohn Sham equations.

Basis sets

Plane waves

Although real space grid methods, akin to the finite element method, may be used to solve the Kohn-Sham equation, the Kohn-Sham orbitals are typically expanded using a basis set. The plane wave (PW) basis is perhaps the most common for periodic calculations, as well as being effective for atomic and molecular systems. It is an orthonormal and in principle, complete, basis set that has the advantage of being universal. In practice the expansion must be truncated, however the only parameter that needs to

be adjusted to the system is the cutoff energy, which defines the smallest reciprocal lattice vector to be expanded:

$$E_{\text{cut}} = \frac{\hbar^2 |k + G_{\text{min}}|^2}{2m}. \tag{3.20}$$

The largest reciprocal lattice vector is naturally determined by the size of the unit cell or, in the case of lower dimensional systems, the simulation cell. Further, the formulation of DFT in this basis is the simplest and can be quite easily and efficiently be parallelised for large calculations. On the other hand, core states cannot be included as extremely high numbers of plane waves are required to reproduce the rapid oscillation of these deep levels. An effective core pseudopotential must therefore be used in conjunction with the basis set. The calculation of non-local exchange, required for the hybrid density functionals that will be discussed in the following section, is also very expensive using this basis.

Localised basis sets - Gaussian type functions

An alternative approach has its roots in the so-called linear combination of atomic orbitals (LCAO) method. In principle this is most rigorously done by using Slater-type orbitals (STO), analytical solutions of the Schrödinger equation for the single electron atoms. However, these functions are comparatively difficult to integrate, even numerically.

A common alternative is the use of a superposition, or linear combination, of Gaussian functions to approximate the atomic orbitals. Multi-centred integrals of these functions may calculated analytically by using the Gaussian product theorem:

$$
\begin{aligned}
g_1(\mathbf{r})g_2(\mathbf{r}) &= e^{-\alpha(\mathbf{r}-\mathbf{R}_1)^2} \cdot e^{-\beta(\mathbf{r}-\mathbf{R}_2)^2}, \\
&= e^{-\frac{\alpha\beta}{\alpha+\beta}(\mathbf{R}_1-\mathbf{R}_2)^2} e^{-(\alpha+\beta)(\mathbf{r}-\mathbf{P})^2},
\end{aligned} \tag{3.21}
$$

where $\mathbf{P} = (\alpha\mathbf{R}_1 + \beta\mathbf{R}_2)/(\alpha+\beta)$ is the centre of mass. This may be implemented in a very computationally efficient manner, for which reason this approach has been favoured in quantum chemistry for many decades. Basis functions of this type are commonly referred to as Gaussian-type orbitals (GTO) or, more correctly, Gaussian-type functions (GTF). Using a Cartesian system, the basis functions are of the form

$$
g_\mu(\mathbf{r}) = x^i y^j z^k e^{-\alpha_\mu(x^2+y^2+z^2)}, \tag{3.22}
$$

where $l = i + j + k$ is the angular momentum quantum number and α_μ, the exponent, is a parameter controlling the width of the function, such that the function becomes more diffuse ("spread out") as $\alpha_\mu \to 0$.

Alternatively, one may define spherical basis functions of the form

$$
g_\mu(\mathbf{r}) = Y_{lm}(\theta,\phi) r^{n-1} e^{-\alpha_\mu \mathbf{r}^2}, \tag{3.23}
$$

where n, l, and m are respectively the principal, angular momentum, and magnetic quantum numbers, and $Y_{lm}(\theta,\phi)$ are spherical harmonics.

A basis set consisting of only a single primitive GTF per angular momentum (s, p, d, f, etc.) is known as a minimal basis set. Such basis sets are inadequate for producing research quality results. Instead, the atomic or-

bitals are typically composed of a linear combination of N basis functions, such that

$$\varphi_\nu^{AO}(\mathbf{r}) = \sum_\mu^N c_\mu g_\mu(\mathbf{r}), \tag{3.24}$$

where c_μ are normalisation coefficients. Such functions are known as *contracted* GTOs or GTFs. The quality of the basis set is labelled by the number of primitive GTFs used to describe each AO. A basis set consisting of two primitive GTFs per AO is labelled double-zeta, while one comprising three primitive GTFs per AO is labelled tripled-zeta, and so on.

This is arguably the most popular choice of basis set for atomic and molecular calculations. However, GTFs may also be extended to periodic systems by the use of Bloch's theorem, such that

$$\phi_\nu(\mathbf{r}, \mathbf{k}) = \sum_g e^{i\mathbf{k}\cdot\mathbf{g}} \varphi_\nu^{AO}(\mathbf{r} - \mathbf{A}_\nu - \mathbf{g}), \tag{3.25}$$

where $\mathbf{g}$ are the lattice translation vectors and $\mathbf{A}_\nu$ is the position of the ν^{th} atom in the primitive cell, on which the ν^{th} AO is centered. The crystalline orbitals (COs) are in turn expanded as a linear combination of the Bloch functions

$$\psi_i^{CO}(\mathbf{r}, \mathbf{k}) = \sum_\nu a_{\nu i}(\mathbf{k}) \phi_\nu(\mathbf{r}, \mathbf{k}), \tag{3.26}$$

where a_{ij} are coefficients to be obtained by the self-consistent solution of the Hartree-Fock or Kohn-Sham equations, analogous to the Fourier coefficients of the PW method.

The main disadvantage over the PW method is that the basis functions are not orthogonal and there is no universal GTF basis set. An atomic basis set that performs well for an atom in one particular molecule may be

entirely inadequate when used for the same species in a different molecule. Moreover, basis sets optimised for molecular calculations are generally unsuitable for solid state calculations without at least some level of modification, typically by reoptimising the exponents of the most diffuse primitive functions or removing them completely.

However, the fact that only a few basis functions are required to represent each electron means that all electron calculations are entirely practical, even for systems containing 4^{th}or 5^{th}row elements. This notwithstanding, it is still possible to use pseudopotentials and only include valence electrons in the basis set, which is commonly done for large systems involving heavier atoms in order to reduce the calculation time. This can have the added advantage of encapsulating relativistic effects, including *s* orbital contraction and spin-orbit coupling, in the frozen core electrons.

Basis set superposition error

One disadvantage of the use of localised basis sets is the issue of basis set superposition error (BSSE), which arises from the use of basis sets that are not complete. This occurs when some of the basis functions of two or more adjacent atoms overlap, causing these atoms to extend their own basis sets with the overlapping functions. This typically results in the prediction of higher total energies, which can be a serious problem when taking relative energy differences, such as in the calculation of disassociation or adsorption energies. The effect diminishes as the complete basis set limit is approached, however computational expense typically limits the size of basis sets used. A commonly used method for computing the BSSE is the counterpoise method [136].

Limitations of DFT

Despite the many successes of DFT, a number of material properties still remain out of reach and the approximation fails catastrophically for certain classes of system. For example, so-called "strongly correlated" systems are well known to be poorly described by conventional exchange-correlation functionals. Of particular pertinence to this work, it is well known that Kohn-Sham DFT systematically and usually grossly underestimates the energy gap (between the highest occupied and lowest unoccupied states) of semiconducting and insulating materials [137].

Self-interaction

One source of error arises from local and semi-local approximations to the exchange-correlation potential. As the effective potential is a functional of the total charge density, this results in the nonphysical situation that each electron interacts with all N electrons in the system, including itself, an artefact known as the self-interaction. This has the effect of increasing the eigenvalues of the occupied orbitals (but not the unoccupied, or "virtual", orbitals), resulting in the prediction of too small an energy gap and in extreme cases, even nonphysical metallic occupancies.

Self interaction correction (SIC) methods were developed in the early 1980s [138]. These are typically of the form

$$E_{\mathrm{xc}}^{\mathrm{SIC}}[\rho] = E_{\mathrm{xc}}[\rho] - \sum_{i}^{N} \left[\int \int \frac{\rho_i(\mathbf{r}_1)\rho_i(\mathbf{r}_2)}{|\mathbf{r}_1 - \mathbf{r}_2|} \mathrm{d}\mathbf{r}_1 \mathrm{d}\mathbf{r}_2 + \int \rho_i(\mathbf{r}_1) \epsilon_{\mathrm{xc}}[\rho_i, 0] \mathrm{d}\mathbf{r}_1 \right]. \tag{3.27}$$

It is worth noting that self-interaction is also present in Hartree-Fock theory, in which the case the unoccupied orbitals are affected but the occupied orbitals are not, due to the cancellation of the exchange and Hartree energies. The consequences of this are discussed in section 3.5.2.

The derivative discontinuity

The Kohn-Sham eigenvalue spectrum pertains to the set of one-electron orbitals of the non-interacting auxiliary system and hence those of the unoccupied, or virtual, orbitals are not the excitation energies. That the eigenvalues approximate in any way the excitation spectrum of the true interacting system has been the subject of considerable speculation and research [139, 140]. Indeed, the only eigenvalue which is directly related to the corresponding interacting system is that of the highest occupied orbital in the ground state. In the case of the exact density functional, this is the negative of the first ionisation potential, $I(N)$.

The energy gap is defined as the difference between the first ionisation potential and the electron affinity:

$$E_g = I(N) - A(N), \tag{3.28}$$

where $I(N) = E(N) - E(N-1)$ is the energy required to remove an electron from the system and $A(N) = E(N+1) - E(N)$ is the energy required to add an electron to the system. However, the Kohn-Sham gap is simply the difference between the eigenvalues of the lowest unoccupied and highest occupied orbitals:

$$E_g^{KS} = E_{N+1}(N) - E_N(N). \tag{3.29}$$

As mentioned above, $E_N(N) = -I(N)$, were the exact density functional known and used, however $E_{N+1}(N) \neq -A(N)$. The difference arises from the discontinuity in the functional derivative of the exchange-correlation energy:

$$\Delta_{KS} = \lim_{\delta \to 0} \left[\left. \frac{\delta E_{\mathrm{xc}}[N]}{\delta n(\mathbf{r})} \right|_{N-\delta} - \left. \frac{\delta E_{\mathrm{xc}}[N]}{\delta n(\mathbf{r})} \right|_{N+\delta} \right] \tag{3.30}$$

The "true" energy gap is therefore:

$$E_g = E_g^{KS} + \Delta_{KS} \tag{3.31}$$

HYBRID DFT

The adiabatic connection

It is naturally desirable to find a means of overcoming the limitation of prediction of material band gaps. A number of methods can be used to do this with varying limitations and levels of success. One of the most common and successful tools is the GW approximation, which is a many body theory that may be implemented self-consistently or as a perturbation. However, it is very expensive to compute for all but small systems.

An alternative and promising, if controversial amongst purists, approach is the use of hybrid density functionals. In this case, the exchange correlation functional is modified to include a certain fraction of exact exchange energy calculated in the Hartree-Fock formalism. These functionals were originally developed in order to improve thermal chemistry calculations,

but have been shown to in some way counteract the effects of the self-interaction. The justification for this is based upon the *adiabatic connection*.

The aim of the adiabatic connection is to achieve a continuous transformation, by means of a coupling constant λ, between the non-interacting auxiliary system and the fully interacting physical system [141, 142]. The Hamiltonian is modified such that

$$H = T + \lambda V_{ee} + V_{ext}^{\lambda}. \tag{3.32}$$

The external potential V_{ext}^{λ} serves to constrain the density of both systems to be equal. The adiabatic connection formula is given by

$$E_{xc} = \int_0^1 \frac{dE_{xc}^{\lambda}}{d\lambda} d\lambda, \tag{3.33}$$

where

$$E_{xc}^{\lambda} = \langle \Psi_{\lambda} | V_{ee}^{\lambda} | \Psi_{\lambda} \rangle - E_H. \tag{3.34}$$

For $\lambda = 1$, the fully interacting system is recovered, while as $\lambda \to 0$ the Coulomb repulsion term is reduced to o and therefore $E_{xc} \to E_x$. It follows that E_{xc} falls between these limits according to the functional used [143].

Hybrid density functionals

Theoretically grounded in the adiabatic connection, hybrid functionals combine exact exchange calculated in an analogue to the Hartree-Fock formalism with approximate exchange and correlation from DFT.

Interestingly, Kohn and Sham discuss the use of such a hybrid methodology in their original paper, referring to it as a "Hartree-Fock method corrected for correlation effects" [133]. This method has been shown to provide accurate prediction of energy gaps for a number of common semiconductors and oxides, but at significantly less computational expense than many-body perturbation methods such as GW [18, 19, 144].

PBE0 & B3LYP

A large number of hybrid functionals exist, of which one of the most common, PBE0, takes the form

$$E_{xc}^{PBE0} = E_{xc}^{PBE} + 0.25(E_x^{HF} - E_x^{PBE}), \tag{3.35}$$

where E_{xc}^{PBE} is the PBE exchange-correlation energy and E_x^{HF} and E_x^{PBE} are the Hartree-Fock and PBE exchange energies, respectively [145]. This functional is based on a rigorous analysis of the adiabatic connection and DFT calculations employing it are still truly *ab initio*.

A wider class of hybrid functionals are parameterised to fit sets of experimental data, including one of the earliest and equally popular, B3LYP. This more complicated functional blends Hartree-Fock exact exchange with both LDA and GGA exchange and correlation energies:

$$\begin{aligned} E_{xc}^{B3LYP} =& E_{xc}^{LDA} + 0.2(E_x^{HF} - E_x^{LDA}) + 0.72(E_x^{GGA} - E_x^{LDA}) \\ &+ 0.81(E_c^{GGA} - E_c^{LDA}), \end{aligned} \tag{3.36}$$

where E_x^{LDA}, E_c^{LDA}, E_x^{GGA}, and E_c^{GGA} are the LDA and GGA exchange and correlation terms, respectively [146]. The original purpose of this functional was to improve ground state energies for thermochemistry calculations.

Range-separated functionals

A further class of hybrid functionals are range-separated and typically also parameterised. Of particular interest are the HSEox screened Coulomb potential functionals [147, 148]. The exchange energy is split into short and long range terms, with Hartree-Fock exact exchange only calculated at short range. The rationale for this approximation is that the electron-electron Coulomb interaction is screened and that beyond this screening length, each electron only "sees" the average charge density. The functionals are of the form

$$E_{xc}^{HSE} = aE_x^{HF,SR}(\omega) + (1-a)E_x^{PBE,SR}(\omega) + E_x^{PBE,LR}(\omega) + E_c^{PBE}, \qquad (3.37)$$

where $E_x^{HF,SR}(\omega)$ is the short ranged Hartree-Fock exact exchange energy, $E_x^{PBE,SR}(\omega)$ and $E_x^{PBE,LR}(\omega)$ are the short and long ranged PBE exchange energies, a is the fraction of exact exchange to be incorporated, and ω is the screening parameter. For HSE03 $a = 0.25$ and $\omega = 0.3$, while for HSE06 $a = 0.25$ and $\omega = 0.2$.

Ab initio or semi-empirical?

Further debate exists, especially in the computational condensed matter physics community, over whether calculations made using hybrid func-

tionals are truly *ab initio* or rather semi-empirical. In the case of the range-separated HSE functionals and B3LYP, and indeed the semi-local BLYP functional on which it is based, their dependence on a number of parameters most certainly puts them in the latter category. From a purist's point of view this is undesirable, although their effectiveness for a large number of systems all but quells any such concerns in practical use.

On the other hand, the rigorous mathematical analysis leading to the single parameter of the PBE0 functional suggest that it can justifiably be described as *ab initio*.

TIME-DEPENDENT DENSITY FUNCTIONAL THEORY

Runge-Gross theorem and the time-dependent Kohn-Sham equations

Although in subsections 3.5.1 and 3.5.2 justification was given for interpreting the single-particle gap as the fundamental energy gap, it is accepted that, at least in the Kohn-Sham formalism[1], DFT is solely a ground-state theory. The prediction of excited-state properties, such as the optical response, is therefore precluded. To deal with such properties, a time-dependent scalar potential and corresponding time-dependent density must be introduced. In an analogue to the first Hohenberg-Kohn theorem, the Runge-Gross theorem states that there is a one-to-one mapping between these two quantities, *up to* a time-dependent constant [149]. This caveat arises from the fact that two potentials differing by only a time-dependent constant produce the same wavefunction differing by only a

1 The mapping between wavefunction and density of the Hohenberg-Kohn theorems in principal extends to excited states.

time-dependent phase factor, which cancel out by means of complex conjugation when taking expectation values.

There is no variational principle for time-dependent systems, therefore the derivation of the time-dependent Kohn-Sham equation considers the action [150]

$$A[\Psi(t)] = \int_{t_0}^{t_1} \langle \Psi(t)| \, i\partial_t - \hat{H}(t) \, |\Psi(t)\rangle \, \mathrm{d}t. \tag{3.38}$$

The time-dependent Kohn-Sham equations are

$$\left[-\frac{1}{2}\nabla_i^2 + V_{\text{eff}}^{(i)}(\mathbf{r}, t) \right] \phi_i(\mathbf{r}, t) = i\frac{\partial}{\partial t}\phi_i(\mathbf{r}, t). \tag{3.39}$$

The time-dependent density is constructed from the time-dependent Kohn-Sham orbitals, such that

$$\rho(\mathbf{r}, t) = \sum_i |\phi_{KS}^{(i)}(\mathbf{r}, t)|^2. \tag{3.40}$$

4

METHODOLOGY

LOCALISED BASIS SET CALCULATIONS

As discussed in subsection 3.4.3.2 of the preceding chapter, the choice of Gaussian-type orbitals (GTO) as basis functions allows the use of all-electronic basis sets as well as the efficient calculation of nonlocal exchange, both of which were desired for this study. The unfortunate drawback over PW and related methods is that no universal GTO basis set exists, therefore sets must be chosen to suit the system being considered. Indeed, the selection of a suitable basis set is critical to producing good results. For materials which have been studied experimentally, it is common to choose sets that closely reproduce measured results. Existing experimental data on GO is unfortunately of limited use to this end. However, previously published *ab initio* calculations provide a useful starting point, in particular those presented in Ref. [95]. These calculations were performed using the GPAW code, an implementation of the projector-augment wave (PAW) method.

With this set of reference calculations in place, a number of published molecular basis sets for C and O were tested for their ability to reproduce

these results. Atomic calculations were performed first to provide the C and O ground state energies required for the calculation of binding energies, followed by simulations of graphene and partially oxidised graphene. A published study of graphane and fluorographene using GTOs examined and compared the use of Pople split valence and Dunning correlation-consistent basis sets of various quality with considerable success [151]. Basis sets of these types were therefore chosen for testing.

For atomic C and the C_2 molecule, the 6-311G* [152] split valence and cc-pCVDZ [153] basis sets, as well as a minimal set from an unpublished study of carbon nanotubes, were tested. For atomic O, 6-311G*, 6-31G(3df,3pd) [154], 8-411d11G [155] and cc-pCVDZ basis set were tested. The same basis sets were then used to simulate graphene, atomic O adsorbed on graphene supercells of varying size, and O dimers, trimers, and tetramers adsorbed on a graphene supercell of 32 C atoms.

Use of the cc-pCVDZ basis set for both atoms was found to reproduce the reference calculations most faithfully, with the calculated binding energies and bond lengths found to be in excellent agreement, as reported in section 5.2. This basis set has also been used for the parameterisation of molecular dynamics simulations of GO [156]. However, when moving to fully oxidised graphene linear dependency and "charge-sloshing" problems were encountered. The most diffuse C orbital, a polarisation function, was found to be the source of the problem, due to overlap with an O orbital. The solution was to simply increase and then reoptimise the exponent of this Gaussian function. The previous calculations were repeated to ensure consistency, with only very small differences as a result. The modified C basis set, following convention, is thus noted m-cc-pCVDZ and is printed in full in the appropriate format for the CRYSTAL code in appendix A.

CALCULATION OF STRUCTURAL PROPERTIES

The calculation of structural properties was carried out at the generalised gradient approximation (GGA) level of theory using the PBE exchange-correlation functional. Geometry optimisation calculations were performed using the Broyden-Fletcher-Goldfarb-Shanno (BFGS) algorithm, a quasi-Newton method [157–160]. The energy convergence tolerance between optimisation steps was set at 10^{-7} Ha ($\sim 10^{-6}$ eV), with the maximum atomic displacement set at 0.01 Å. A Monkhorst-Pack shrinking factor of 2×2 was used to determine the number of sampling points in the IBZ [161]. Integration in real space was performed on a grid of 75 radial points by 974 angular points. A high level of Kohn-Sham density matrix mixing of 80%, in conjunction with Anderson's method [162] for convergence acceleration, was employed throughout.

The binding energy per O atom was calculated as

$$E_c = \left[E_{C_m} + nE_O - E_{C_mO_n}\right]/n, \tag{4.1}$$

where E_{C_m} is the total energy of a graphene supercell of m C atoms, $E_{C_mO_n}$ is the total energy of the graphene supercell functionalised with n O atoms, and E_O is the ground state energy of a free O atom. The vacancy formation energy, or energy required to remove p O atoms from GO, per O atom, was calculated as

$$E_v = \left[E_{C_mO_n} - \left(E_{C_mO_{n-p}} + pE_O\right)\right]/p. \tag{4.2}$$

CALCULATION OF BSSE

The basis set superposition error (BSSE) associated with the use of localised basis sets can seriously affect the calculation of adsorption energies and it is therefore vital to correct for this. The BSSE was therefore calculated using the counterpoise method [136]. The correction to the binding energy according to this prescription is

$$\Delta^{\mathrm{CP}} = E^{A}_{AB}(A) - E^{AB}_{AB}(A) + E^{B}_{AB}(B) - E^{AB}_{AB}(B), \tag{4.3}$$

where $E^{z}_{y}(x)$ is the energy of system x calculated at geometry y with basis set z [163]. This is achieved by the use of "ghost" atoms, for which the charge is set equal to zero but the basis set is left in place, giving additional variational freedom to the remaining atoms to extend their basis. The resulting energy contribution can thus be quantified and corrected for.

For a single atom adsorbed on a surface, this calculation is trivial to set up. For calculations involving multiple adsorbates, all but one atom in the supercell is replaced by ghosts. As the ground state of the O atom is $^{3}P_{2}$, the spin configuration for O in the presence of ghost atoms must be modified to reflect this.

CALCULATION OF ELECTRONIC AND OPTICAL PROPERTIES

Electronic and optical properties are calculated using the hybrid DFT approach discussed in section 3.5. The PBE0 [145] and B3LYP [146] functionals are used for both, while results for the former calculated with the HSE06 [18] functional are presented by way of comparison. Similar tol-

erances are used as for the structural calculations, with the exception of an increase of the Monkhorst-Pack scaling factors to 16×16 to give 130 k-points in the IBZ. While interatomic forces and hence structural properties are not very sensitive to the resolution of IBZ sampling, accurate determination of the electronic properties such as the band structure, position of the Fermi level and electronic density of states are strongly affected.

Dipole matrix elements are calculated as

$$\mathbf{p}_{if} = (E_f - E_i)\mathbf{d}_{\mathbf{k}_i \to \mathbf{k}_f}, \tag{4.4}$$

where E_i and E_f are the eigenvalues of the initial and final states involved in the transition and $\mathbf{d}_{\mathbf{k}_i \to \mathbf{k}_f}$ is the vertical transition probability [164]. The latter of these is defined as

$$\mathbf{d}_{\mathbf{k}_i \to \mathbf{k}_f} = i \int \mathrm{d}\mathbf{r}\, u^*_{\mathbf{k}_f}(\mathbf{r}) \nabla_{\mathbf{k}} u_{\mathbf{k}_i}(\mathbf{r}). \tag{4.5}$$

The functions $u_{\mathbf{k}_i}(\mathbf{r})$ and $u_{\mathbf{k}_f}(\mathbf{r})$ are the Bloch functions of the initial and final states, related to the Kohn-Sham orbitals by $\psi_{\mathbf{k}i}(\mathbf{r}) = e^{i\mathbf{k}\cdot\mathbf{r}} u_{\mathbf{k}i}(\mathbf{r})$.

The radiative transition times between the highest occupied and lowest unoccupied states are calculated as

$$\frac{1}{\tau^{rad}_{if}} = \frac{F^2}{3}\alpha \frac{(E_f - E_i)}{\hbar m_0^2 c^2} \sum_{\nu} n_\nu |\hat{\mathbf{e}}_\nu \cdot \mathbf{p}_{if}|^2, \tag{4.6}$$

where α is the fine structure constant, m_0 is the electron rest mass, c is the vacuum speed of light, and $n_\nu \simeq \sqrt{\epsilon_r}$ and $\hat{\mathbf{e}}_\nu$ are respectively the refractive index and light polarisation unit vector along Cartesian direction ν. F is a dielectric screening term, chosen to account for the dielectric environment. The dielectric constant, ϵ_r is calculated using the linear response formalism

of TD-DFT as implemented in a development version of the Crystal 09 code [165].

The absorption cross section is calculated as

$$\sigma(\hbar\omega) = \frac{\pi}{c\epsilon_0\omega}\left(\frac{e}{m_0}\right)^2 \sum_{v,if} \frac{|\hat{\mathbf{e}}_v \cdot \mathbf{p}_{if}|^2}{n_v} G(E_{\mathbf{k}f} - E_{\mathbf{k}i} - \hbar\omega), \tag{4.7}$$

where ϵ_0 is the vacuum permittivity, e is the fundamental electronic charge, ω is the incident photon frequency, and the Gaussian function $G(x) = \exp\left[-\left(x/\sqrt{2}\Delta\right)^2\right] / \left(\sqrt{2\pi}\Delta\right)$ is controlled by the spectral line broadening, Δ. For all absorption calculations Δ is set equal to 50 meV.

METHODOLOGY APPLIED TO III-V SEMICONDUCTORS

The group III-V binary semiconductors and their alloys are the basis of perhaps the majority of current semiconductor and photonics technology and are accordingly well studied. Most of their material properties are well known and therefore represent a good benchmark against which to test the predictive ability of theoretical methods. To this end, extensive calculations were performed on a range of common III-V materials in their zincblende and where appropriate wurtzite crystallisations, using the PBE0 and B3LYP hybrid functionals and the PBE semi-local functional.

Calculated energy gaps of the zincblende crystallised III-V semiconductors from simulations on experimental geometry are presented in Tab. 4.5, along with experimental values for comparison [166, 167].

The systematic and in some cases catastrophic underestimation of energy gaps of DFT at the GGA level of theory is immediately evident, with a mean absolute error (MAE) across this set of materials of 0.988 eV. No-

	E_g^{PBE0} [eV]	E_g^{B3LYP} [eV]	E_g^{PBE} [eV]	E_g^{exp} [eV]
AlAs	2.722	2.705	1.456	2.240
GaAs	1.971	1.422	0.643	1.519
InAs	0.817	0.387	0.000	0.417
AlN (zb)	5.195	5.171	3.321	5.400
GaN (zb)	3.602	3.350	1.850	3.299
InN (zb)	1.005	0.785	0.000	0.780
AlN (wz)	6.605	6.398	3.213	6.250
GaN (wz)	3.787	3.521	2.002	3.510
InN (wz)	1.172	0.934	0.000	0.780
AlP	3.026	3.021	1.698	2.520
GaP	3.014	2.919	1.770	2.350
InP	2.301	1.846	0.980	1.424
AlSb	2.460	2.431	1.296	1.696
GaSb	1.326	0.810	0.185	0.812
InSb	0.874	0.393	0.000	0.235

Table 4.1.: Calculated band gaps of III-V semiconductors on experimental geometry using B3LYP, PBE0, and PBE, with experimental values for comparison.

tably the PBE functional predicts a conducting ground state for three of the Indium containing materials, InAs, InN, and InSb. The values calculated using the hybrid functionals in general compare much more favourably to those obtained from experiment, with a substantially lower mean absolute error (MAE) of 0.473 eV for PBE0 and just 0.224 eV for B3LYP. Most importantly, all ground states are found to be insulating/semi-conducting, including those of InAs, InN, and InSb.

The band structure of InAs calculated using the PBE functional is shown in Fig. 4.1(a), where the conduction band edge at the Γ point is clearly seen to cross the Fermi level and intersect the valence band edge. Fig. 4.1(b)

shows the band structure calculated using B3LYP, with a direct band gap correctly predicted.

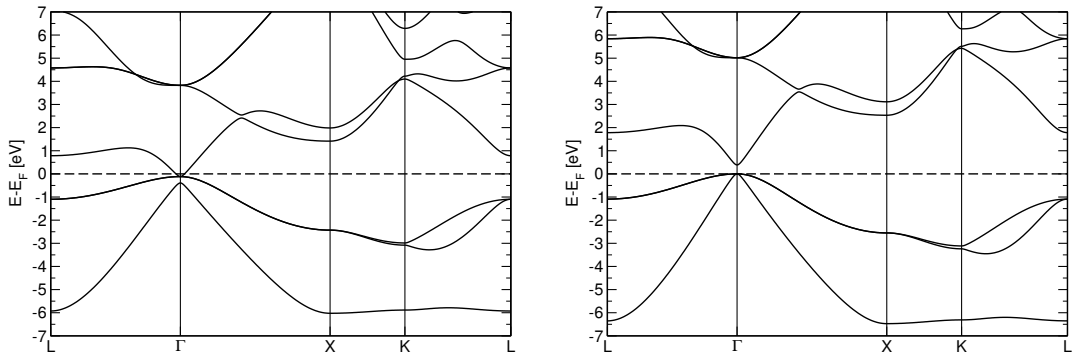

(a) PBE. (b) B3LYP.

Figure 4.1.: Band structure of Indium Arsenide calculated using *ab initio* PBE and hybrid B3LYP functionals. The PBE calculation shows the conduction band edge crossing the Fermi level, while B3LYP correctly predicts a semiconducting ground state.

With the exception of AlN, PBE0 is seen to consistently overestimate band gaps by $\sim$0.5 eV and in the worst case by almost 0.9 eV. The effect is markedly less severe for B3LYP, crucially so in the case of the narrow-gap materials. Although caution must clearly be used in the interpretation of results, this suggests that the use of hybrid DFT can be an effective and efficient method for the prediction of energy gaps and related properties.

5

RESULTS & ANALYSIS

GRAPHENE

The properties of graphene have been intensively studied both experimentally and theoretically, hence there is little to be contributed here. However, adsorption calculations of oxygen on graphene require a geometry optimised ground state calculation. Due to the structure of fully oxidised graphene (GO) adopted for this study, which will be discussed in section 5.3, a supercell of C_{2h}^{y} point group symmetry [2] containing 32 carbon atoms is used, as shown in Fig. 5.1.

The principle components of the elastic tensor, which will later be compared to those of GO, were calculated as c_{11} = 357 Nm^{-1}, c_{22} = 371 Nm^{-1}, c_{12} = 51 Nm^{-1} and c_{66} = 137 Nm^{-1}. The reported experimental value for the in-plane components in graphene obtained by atomic force microscopy is 340 $\pm$ 50 Nm^{-1}, which compares most favourably and lends confidence in the choice of basis set [22, 168].

2 The superscript denotes the alignment of the principle axis.

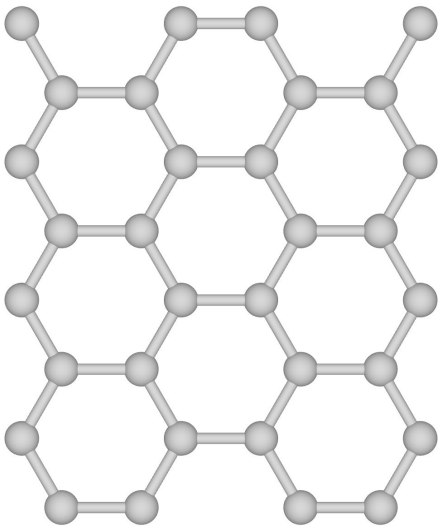

Figure 5.1.: 32 C atom graphene supercell.

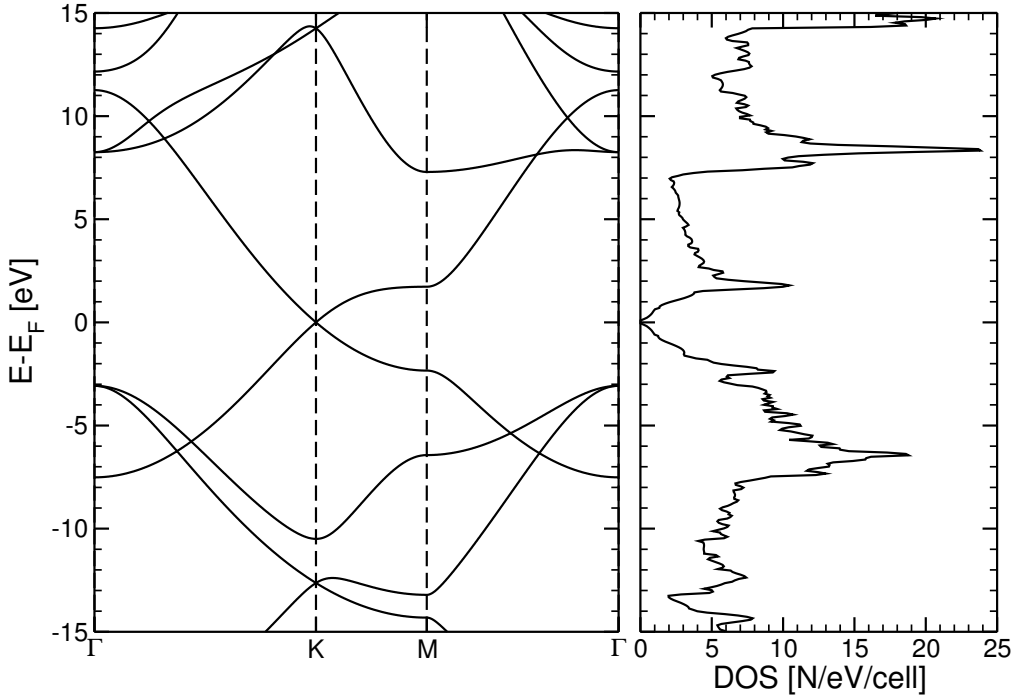

Figure 5.2.: Band structure and density of states of graphene, calculated using PBE on the 32 C atom graphene supercell.

EPOXY FUNCTIONALISATION OF GRAPHENE

It was established in section. 2.3.1 that the graphene oxide produced by "wet chemistry" methods tends to be very defective, therefore suggesting that it is not particularly suited to device applications. On the other hand, promising results have been demonstrated by deposition of atomic oxygen under UHV on to epitaxially grown graphene, which produces epoxy functionalised graphene without damage to the honeycomb lattice [83]. This suggests a more promising route to device applications and is therefore the model of graphene oxide adopted for this study.

To begin studying the properties of GO, calculations were carried out to investigate the epoxy functionalisation of graphene. In the simplest case, a single O atom was placed on a supercell consisting of 32 C atoms and the atomic positions and in-plane lattice parameters relaxed in accordance with the method outlined in chapter 4. A number of starting positions were compared, with the O atom in turn placed above a bridge site, directly above a C atom, and in the middle of an aromatic ring. As expected, in all cases the O atom forms an epoxy functional group at a bridge site upon relaxation, as shown in Fig 5.3 [88, 89]. It is immediately clear that both the D_{6h} point group symmetry of graphene and the C_{2h}^{y} point group of the supercell have been reduced.

The bond energy for this configuration, calculated using Eq. 4.1 relative to an isolated O atom, is 2.234 eV per O atom. Corrected for BSSE, this is reduced to 2.010 eV per O atom, in good agreement with Ref. [95]. The C-C bond length in the epoxy group is increased from the 1.420 Å of free-standing graphene to 1.515 Å, while the C-O bonds are of length 1.464 Å, forming the near equilateral triangle typical of epoxides. The C-C bond

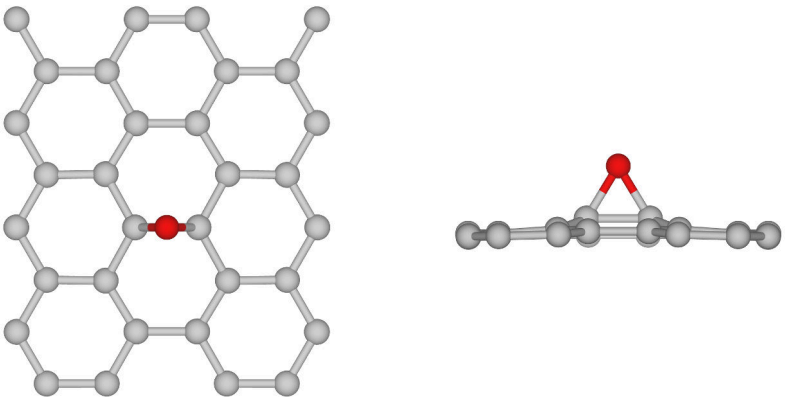

(a) "Top" view. (b) Side view.

Figure 5.3.: Chemisorption of atomic oxygen on graphene, showing vertical displacemnt of C atoms and formation of epoxy functional group.

length is typical for a C-C single bond and is approximately twice the covalent radius of C. The C-C bond length between atoms furthest away from the functionalised site is also increased, this time to 1.430 Å, indicating that the disruption of the π-bonding network has extended effects. The two C atoms of the epoxy ring are displaced vertically by $\sim$0.333 Å from their respective positions in freestanding graphene. This is attributable to the strain induced by the change in bond hybridisation from the sp^2 of pristine graphene to sp^3, analogous to the diamond allotrope [169]. In this case the π-bond between C-$2p_z$ orbitals is broken and two single bonds formed with O-2p orbitals. The symmetry of the sp^3 orbital is typically tetrahedral, giving an angle between lobes of 109.5°. As the O atoms are situated at bridge cites in order to form epoxy moieties, giving a bond angle of 58.8°, this symmetry is broken. This induces strain in the graphene sub-lattice, but is again quite typical of epoxides.

The adsorption of further O atoms greatly increases the number of possible arrangements of adsorbates. However, it has been demonstrated that it is energetically favourable for O adatoms to form clusters on graphene [95].

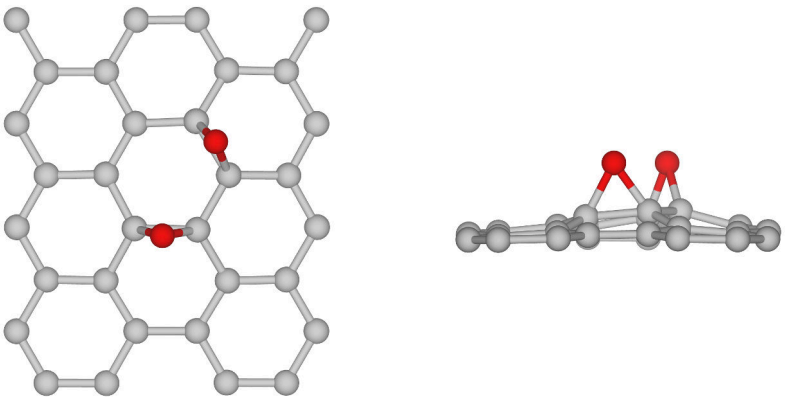

(a) "Top" view. (b) Side view.

Figure 5.4.: Chemisorption of oxygen dimer on graphene, with mutual repulsion of O atoms evident.

Fig. 5.4 depicts one such arrangement. The bond energy for this structure, again calculated relative to an isolated O atom, is 2.416 eV per O atom, or 2.280 eV per O atom after correction for BSSE. The effect of repulsive Coulomb forces between adsorbates is apparent, with the epoxy groups angled away from each other and no longer normal to the plane. The two moieties are not identical, with the C-C bond length of one being 1.515 Å and the other 1.512 Å. The C-O bond lengths are also mismatched, with each functional group having one of 1.440 Å and the other of 1.467 Å of 1.468Å. The increased strain is relaxed by greater vertical displacement of the C atoms, with most shifted by at least 0.100 Å and some as much as 0.480 Å. The C-C bonds furthest from the functional groups are again of length 1.430 Å.

The effects of Coulomb repulsion and lattice distortion are simultaneously minimised when adsorption is alternated above and below the graphene lattice, as shown in Fig 5.5. This structure is more stable with a bond energy of 2.502 eV per O atom and the near identical epoxy functional groups again aligned normal to the graphene lattice. After correction for BSSE the

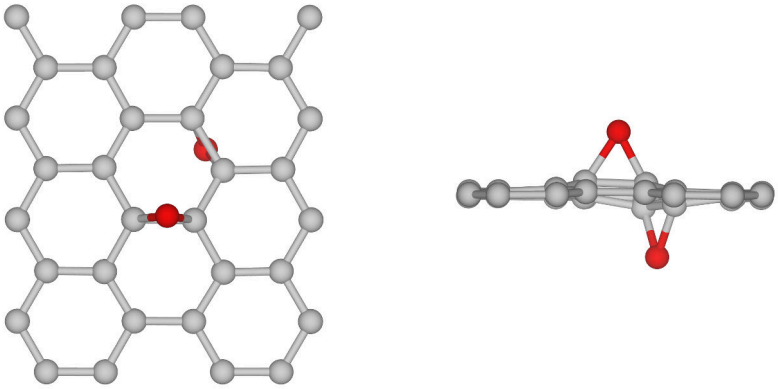

(a) "Top" view. (b) Side view.

Figure 5.5.: Chemisorption of atomic oxygen above and below graphene, minimising repulsion between O atoms and lattice distortion.

bond energy is decreased to 2.366 eV per O atom, again in excellent agreement with Ref. [95]. The C-C bond lengths in the functional groups are shortened to 1.489 Å and 1.490 Å respectively. The two closest C-O bonds are of length 1.454 Å and 1.455 Å respectively, while the opposing two are both of length 1.482 Å. Once again, the C-C bonds away from the functionalised sites are of length 1.430 Å. This alternating of O coverage forms the basis of the model of graphene oxide used in the following sections.

FULLY OXIDISED GRAPHENE

Structural and electronic properties

The most stable structure of fully oxidised graphene [95], as discussed in section 2.3.1, has a unit formula of C_8O_4 and is of C_2^y point group symmetry. The unit cell is depicted in Fig 5.6, in which the O adatoms are seen to each form an epoxy functional group with the two nearest neighbouring C atoms, as with the low O concentration structures in the preceding section.

The C-C bonds in the epoxy moieties are further shortened in comparison to these low coverage structures and are of length 1.477 Å, while the C-O bond lengths of are 1.447 Å, once again forming the near equilateral triangle typical of epoxides. The C-C bonds in between functional groups are of length 1.510 Å in the zigzag direction and 1.508 Å in the armchair direction, again in the range typical of a C-C single bond. As for the structure in Fig. 5.5, the alternation of O coverage above and below the graphene sub-lattice serves to minimise Coulomb repulsion between the adatoms. The nearest neighbouring O atoms, which lay on the same side of the graphene sub-lattice, are separated by 3.383 Å.

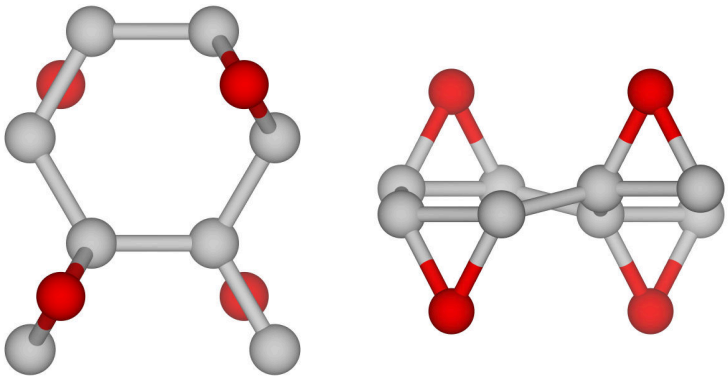

(a) "Top" view. (b) Side view.

Figure 5.6.: Unit cell of graphene oxide, showing alternation of O adsorption above and below graphene lattice.

The vertical displacement of C atoms from their planar hexagonal lattice sites is perfectly balanced by the alternating adsorption arrangement, resulting in a regular corrugation of the graphene sub-lattice, much as observed experimentally [77, 83]. Figure 5.6(b) clearly illustrates this corrugation. In distinction from graphane and partially hydrogenated graphene, however, in which the graphene sub-lattice is greatly distorted in-plane, the hexagonal character is still quite evident. The breaking of all C-C π-bonds

to form single C-C and C-O bonds is readily visualised by comparing the skeletal formula of graphene depicted in Fig. 2.2 with that of the fully epoxy functionalised model of GO shown in Fig. 5.7.

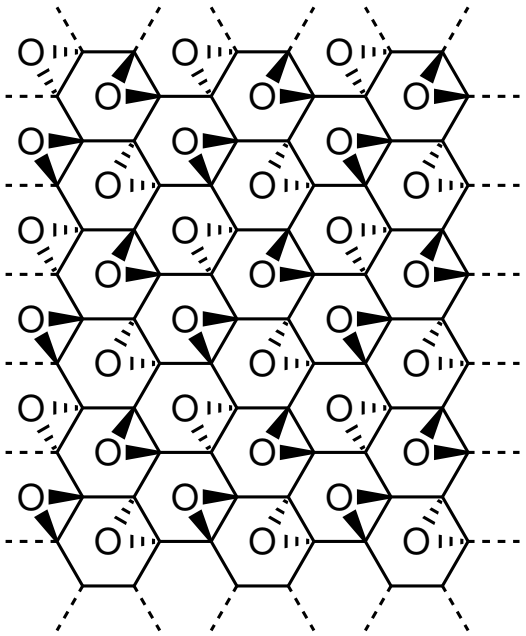

Figure 5.7.: Skeletal formula of graphene oxide.

Important structural properties, calculated using the PBE functional, are presented in Tab. 5.1. The binding energy per O atom of 3.25 eV indicates that the structure is highly stable, which can in part be attributed to the alternating O coverage and the aforementioned resulting relaxation of strain and reduction in electrostatic repulsion. As can be expected because of the complete disruption of the C-C π-bonding network, the principal components of the elastic tensor indicate that GO is substantially softer than graphene. The calculated values of c_{11} and c_{22} compare well to published values of 249.3 Nm^{-1} and 21.2 Nm^{-1} from DFT calculations on a similar epoxy functionalised structure [170].

As it is the C-$2p_z$ π-orbitals that are responsible for the electronic properties in the vicinity of the Fermi level in graphene, the disruption, or in

E_c [eV]	$\bar{r}_{CO}$ [Å]	c_{11} [Nm^{-1}]	c_{12} [Nm^{-1}]	c_{22} [Nm^{-1}]	c_{66} [Nm^{-1}]
3.25	1.45	245	240	25	110

Table 5.1.: Binding energy per O atom, mean C-O bond length and principal components of the elastic tensor of GO.

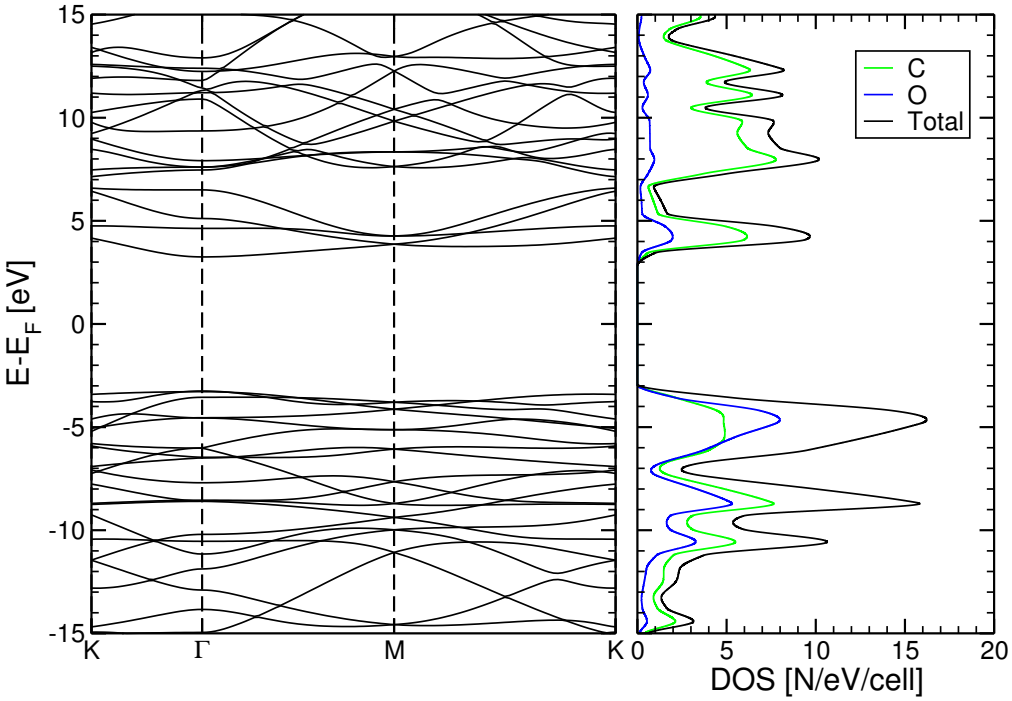

Figure 5.8.: Band structure and density of states calculated with B3LYP. Projected density of states show conduction bands to be dominated by C states.

this case complete removal, of these can be expected to lead to a substantial change of the electronic structure. This is confirmed by the band structure and density of states of GO, shown in Fig. 5.8 from calculations using the B3LYP functional. The characteristic Dirac cones formed by graphene's π and π^* bands intersecting at the Fermi level at the K point are unsurprisingly not present and a substantial band gap of 6.502 eV has been opened, with relatively flat dispersion at the conduction and valence band edges. Effective masses at the conduction and valence band edges are, respectively, $m_e^* = 1.361\ m_0$ and $m_h^* = 0.558\ m_0$ along the $\Gamma \rightarrow$ M direction, and $m_e^* = 0.399\ m_0$ and $m_h^* = 0.442\ m_0$ along the $\Gamma \rightarrow$ K direction. The projected density of states suggest that the highest valence bands can largely be attributed to O-2p states, while the conduction bands are dominated by C-2p states.

Band gaps calculated using the PBE, PBE0, B3LYP, and HSE06 functionals are presented in Tab. 5.2 for comparison. The difference in predictions from *ab initio* and hybrid functionals is quite marked, with the latter all comparing very well to the experimentally observed σ-σ^* transition of 6.53 eV in chemically derived GO [107].

	PBE	PBE0	B3LYP	HSE06
E_g [eV]	4.090	6.850	6.502	6.219

Table 5.2.: Band gap of GO calculated using a range of functionals.

The highest occupied (HOMO) and lowest unoccupied (LUMO) molecular orbitals are presented in Fig. 5.9, with isosurfaces plotted at $\sim$10% of the maximum Kohn-Sham eigenvalues on a 2×2 supercell. Both are seen to be of predominantly sp^3 character, however some contribution from non-

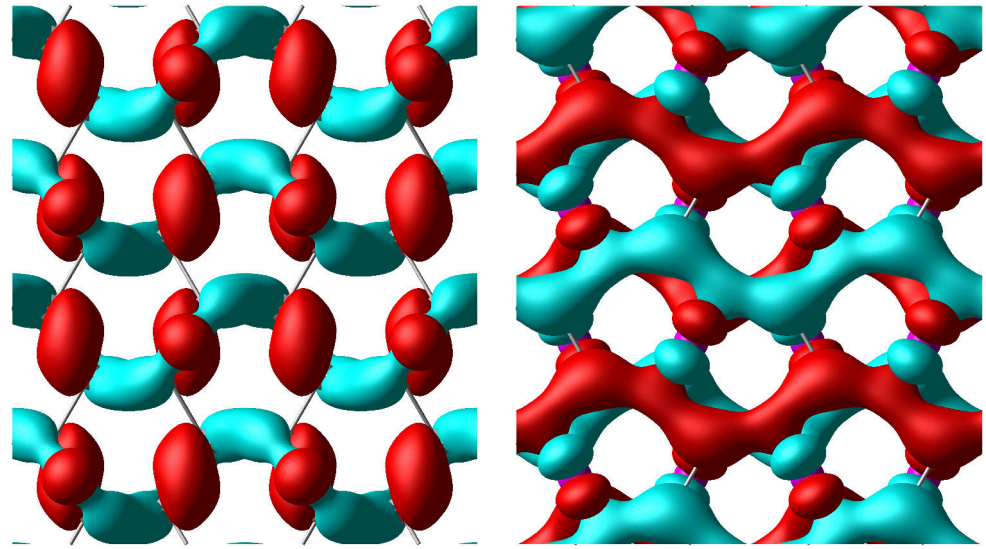

(a) HOMO (xy-plane). (b) LUMO (xy-plane).

(c) HOMO (xz-plane). (d) LUMO (xz-plane).

Figure 5.9.: Highest Occupied and Lowest Unoccupied Molecular Orbitals of GO. The colour denotes the phase of the Bloch wavefunction, with red signifying $+1$ and blue -1. The characteristic lobes of p orbitals are evident on the O atoms.

hybridised O-2p$_z$ (HOMO) and O-2p$_y$ (LUMO) orbitals are evidenced by the distinctive p-orbital lobes on the O atoms.

Absorption properties

As discussed in section 2.3.2 of chapter 2, flakes of GO in aqueous suspension are seen to absorb strongly in the UV range, which corresponds to the σ-σ^* transition, while the absorption peaks shift toward the visible range as the level of oxidation is reduced [171]. Given that the size of the flakes involved in these experiments is too large to expect quantum confinement effects, it is reasonable to assume that the periodic structure considered here should demonstrate similar behaviour, especially given that the predicted σ-σ^* band gap of 6.502 eV is in close agreement with experiment and corresponds to UV photon energies.

	p_x [eV Å]	p_y [eV Å]	p_z [eV Å]	τ_{if}^{rad} [ns]
PBE0	3.880	0	0	2.28
B3LYP	3.656	0	0	2.70

Table 5.3.: Optical dipole matrix elements of GO.

Indeed, calculation of the optical dipole matrix elements of GO, presented in Tab. 5.3, confirms that the direct band gap is optically active, albeit only for x-polarised light. Explanation of the optical properties can be greatly aided by an analysis of the symmetry in accordance with group theory.

	E	C_2^y	linear, rotations	quadratic
A	1	1	y, R_y	x^2, y^2, z^2, xz
B	1	-1	x, z, R_x, R_z	xy, yz

Table 5.4.: C_2^y character table.

According to the character table of the material's C_2^y point group (see Tab. 5.4), there are two irreducible representations (irreps), A and B, the former of which is symmetric with respect to rotation about the principle axis and the latter antisymmetric. Inspection of Fig. 5.9 reveals that HOMO is of irrep A and LUMO is of irrep B.

	A	B
A	A	B
B	B	A

Table 5.5.: C_2 product table.

The Cartesian components of the dipole operator simply transform as the coordinates, such that μ_y is of irrep A and μ_x and μ_z are of irrep B. The selection rules for the two irreps allow for dipole transitions of either exclusively y- or both x- and z- polarisations. The fact that $p_z = 0$ in this case suggests that this polarised transition is forbidden by selection rule.

	ϵ_{xx}	ϵ_{yy}	ϵ_{zz}
B3LYP	1.291	1.387	1.087
PBE0	1.261	1.346	1.078

Table 5.6.: Principal components of the dielectric tensor of GO.

Calculation of the principal components of the dielectric tensor, presented in Tab. 5.6 show GO to be optically anisotropic, as expected [172].

REDUCED GRAPHENE OXIDE

Structural and electronic properties

As discussed in section 2.3.1, reduced graphene oxide (rGO) produced by wet synthesis typically consists of islands of defective sp^2 hybridised graphene surrounded by epoxy, hydroxyl, carboxyl and carbonyl functionalised graphene with a high fraction of sp^3 hybridised bonds. This range of functional groups and defects is attributed to the harsh chemistry involved in the common "top-down" methods employed in its synthesis. For most of this study a model of purely epoxy functionalised graphene, as though synthesised by a "bottom-up" such as that described in Ref. [85], is employed. To simulate rGO, O adatoms are systematically removed from a supercell of either 2×2 or 4×3 GO unit cells, ranging from a single O atom to 4 O atoms for the smaller supercell and 1 to 12 O atoms for the larger. The O atoms are removed in "clusters" to form regions of free graphene, or graphene quantum dots, embedded in the GO lattice. In order to demonstrate that the model is also representative of wet synthesised rGO, a smaller number of simulations including hydroxyl moieties are performed and results compared.

32 C atom supercells

For the 2×2 supercells, all O atoms are removed to form an approximately circular GQD, as shown in Fig. 5.10. Binding energies per O atom and vacancy formation energies for each supercell, calculated after structural relaxation, are presented with and without the counterpoise correction for BSSE in Tab 5.7.

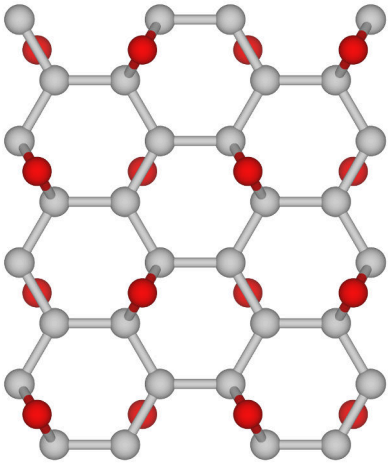

(a) Fully oxidised.

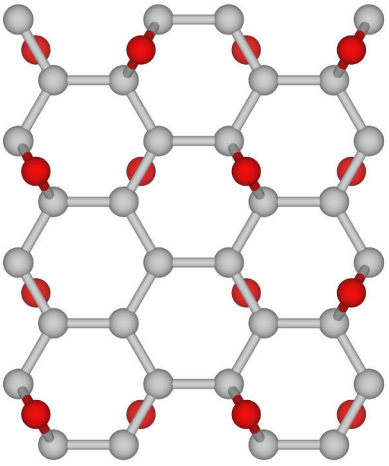

(b) 1 O vacancy.

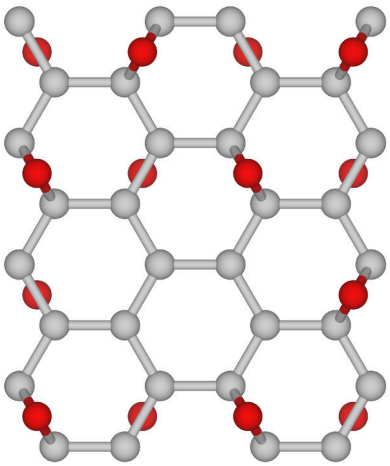

(c) 2 O vacancies.

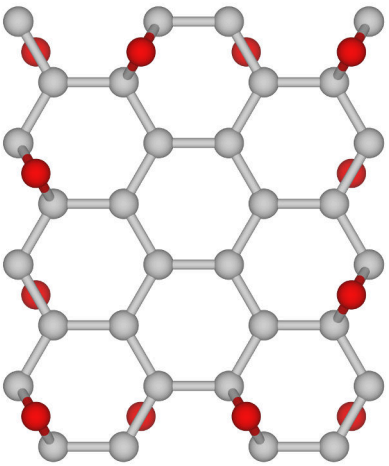

(d) 4 O vacancies.

Figure 5.10.: 2×2 supercell rGO structures.

n_{vac}	0	1	2	4
E_c [eV]	3.378	3.321	3.273	3.176
E_c^{CP} [eV]	3.321	3.263	3.214	3.114
E_f [eV]	n/a	4.240	4.115	3.986
E_f^{CP} [eV]	n/a	4.054	4.024	3.941

Table 5.7.: Binding energy per O atom (Eq. 4.1) and vacancy formation energy (Eq. 4.2)of GO and rGO for 2×2 supercells. The superscript CP denotes that the counterpoise correction for BSSE (Eq. 4.3) has been applied.

The structures are all thermodynamically very stable, although it can be seen that the relative stability is decreased as adsorbates are removed. The importance of computing the BSSE is also quite apparent. Most interesting are the energy gaps, presented in Tab. 5.8. They appear to fit a very simple exponential relationship based on the number of O adatoms removed from GO, such that

$$E_g(n_v) \approx E_g(0) \exp(-0.25 n_v), \tag{5.1}$$

where $E_g(0)$ is the band gap of fully oxidised graphene and n_v is the number of O atoms removed. However, the number of structures is too small to determine the veracity of the fit. To do this it is necessary to see whether the trend continues with increasing size of the free graphene region. The 2×2 supercell is not large enough to accommodate this, therefore the study proceeds using a larger 4×3 GO supercell.

n_{vac}	0	1	2	4
E_g [eV] (PBE0)	6.850	5.241	4.130	2.397
E_g [eV] (B3LYP)	6.502	4.895	3.805	2.143

Table 5.8.: Energy gaps of GO and rGO for 2×2 supercells.

96 C atom supercells

For the larger supercells, the number of possible geometric arrangements naturally increases with the number of O atoms removed. A number of such arrangements were simulated and bonding and vacancy deformation energies calculated and compared [173]. The most energetically favourable configurations of these GQD structures, which also happen to be the arrangements of highest symmetry, are depicted in Fig. 5.11. The C atoms that are not functionalised are coloured darker for distinction.

n_{vac}	0	1	2	4	8	12
E_c [eV]	3.378	3.360	3.346	3.322	3.278	3.216
E_c^{CP} [eV]	3.324	3.306	3.292	3.278	3.228	3.161
E_f [eV]	n/a	4.231	4.119	3.996	3.877	3.865
E_f^{CP} [eV]	n/a	4.181	4.069	3.947	3.856	3.815

Table 5.9.: Binding energy per O atom and vacancy formation energy of GO and rGO for 4×3 supercells. The superscript CP denotes that the counterpoise correction for BSSE has been applied.

The binding energy and vacancy formation per O atom for each of these structures are presented in Tab. 5.9, along with the binding energy of GO for comparison. The values calculated for the structures with 1, 2, and 4 O atoms removed are larger than their counterparts from the 2×2 supercell simulations. The difference increases with the number of O atoms removed,

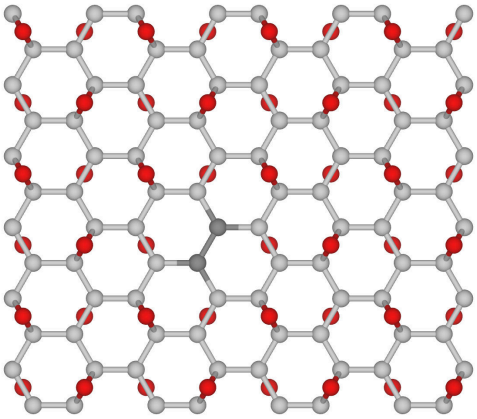

(a) 1 O vacancy.

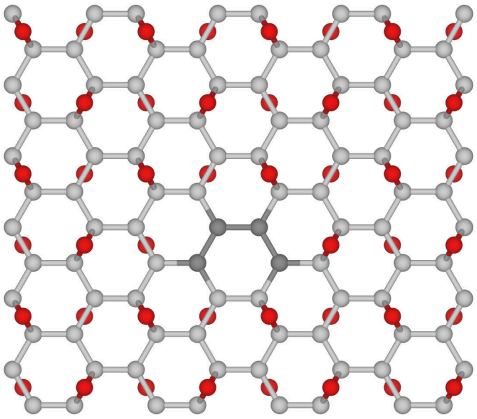

(b) 2 O vacancies.

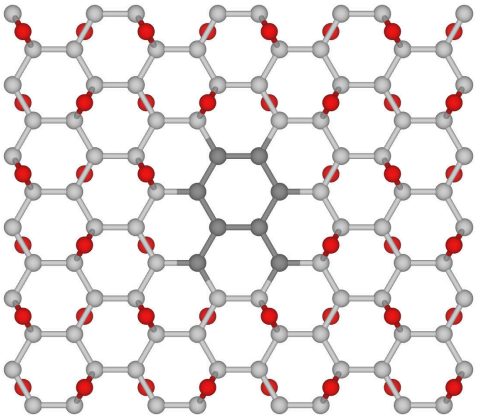

(c) 4 O vacancies.

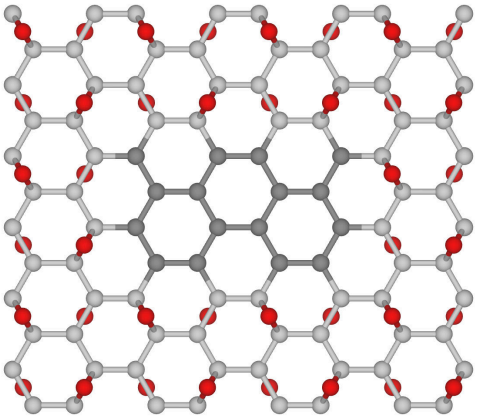

(d) 8 O vacancies.

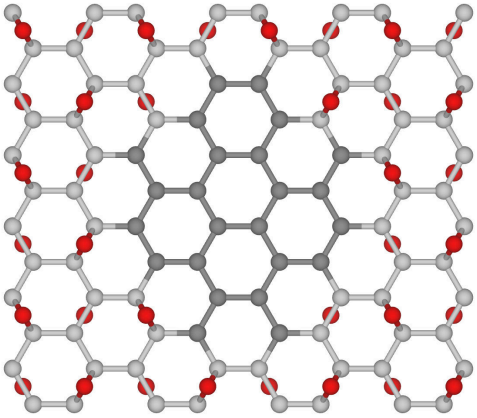

(e) 12 O vacancies.

Figure 5.11.: Most stable structures with n O atoms removed, with C atoms in free graphene regions coloured darker for clarity.

from 0.039 eV to 0.146 eV, which can likely be explained by the greater separation between free graphene regions. The counterpoise correction for BSSE is much smaller, amounting to ∼0.05 eV in all cases.

The local restoration of sp^2 hybridised orbitals and associated π bonds in the non-functionalised regions allows the C atoms to relax to the planar hexagonal lattice sites, creating islands of "clean" graphene. This is depicted very clearly in Fig. 5.12. Along with experimental observations of nanometre scale sp^2 domains in rGO [75], this lends further weight to the Lerf-Klinowski model of GO [72].

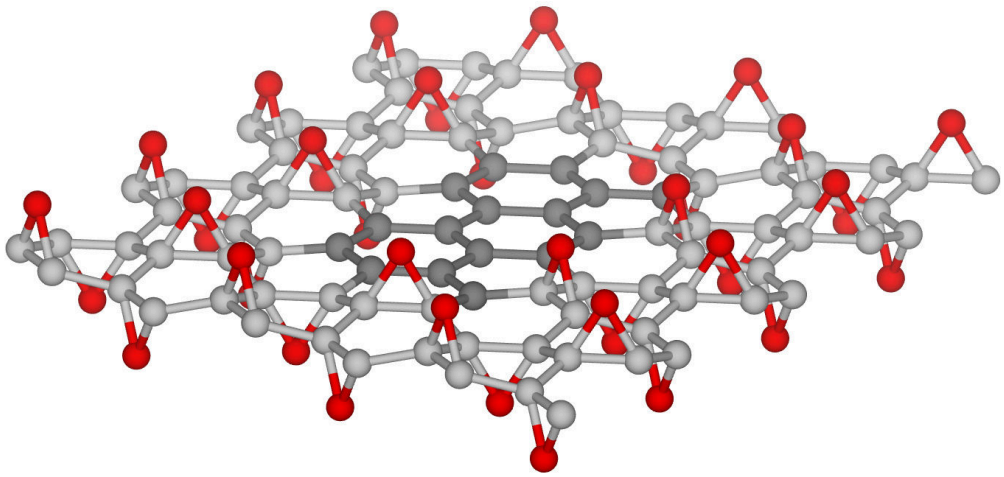

Figure 5.12.: Projection of structure with 8 O vacancies. Relaxation of vertical displacement of C atoms in the free graphene region is clearly evident.

Energy gaps calculated using GGA (PBE) and hybrid functionals are presented for GO and the five most stable rGO structures in Tab. 5.10. As expected, there is a large difference in the predictions made by the two levels of theory. The PBE energy gap for GO falls approximately in the middle of the range of GGA predictions for high O coverage GO reviewed in chapter 2, from ∼3 eV to 4.8 eV [89, 90, 94, 95]. Of greatest significance, at

the lowest level of coverage (12 O atoms removed) where PBE0 and B3LYP predict an energy gap of ∼0.3 eV, PBE predicts a conducting ground state.

n_{vac}	0	1	2	4	8	12
E_g [eV] (PBE)	4.090	3.238	2.502	1.249	0.372	0.000
E_g [eV] (PBE0)	6.850	5.397	4.264	2.594	1.056	0.338
E_g [eV] (B3LYP)	6.502	5.038	3.927	2.327	0.902	0.258

Table 5.10.: Energy gaps of GO and rGO.

The energy gaps predicted by the hybrid functionals do indeed fit well to the relationship, Eq. 5.1, predicted from the 2×2 supercell calculations. This function is plotted with the calculated gaps overlaid in Fig. 5.13. Of course, it must be noted that the asymptotic behaviour of this function is unphysical.

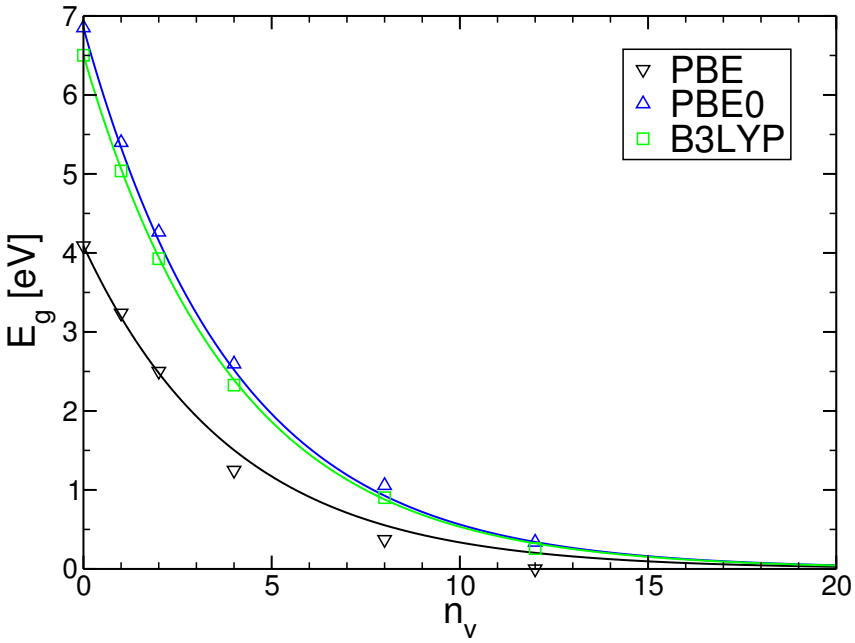

Figure 5.13.: Energy gap vs. no. of O vacancies for the most stable structures of rGO. Symbols depict values of E_g from DFT calculations and solid lines are plots of Eq. 5.1.

A clearer picture of the evolving electronic structure and the origin of the energy gap can be gained from looking at the electron density of states, Fig. 5.14. It is immediately apparent that the highest occupied and lowest unoccupied sp^3 orbitals are little affected by the removal of O atoms. In fact, the gap between the two is slightly widened over that of GO but remains almost constant at $\sim$7 eV. This again falls nicely in line with experimental measurements of the σ-σ^* gap. What changes more noticeably is the emergence of states within the σ-σ^* gap associated with the local restoration of π bonds accompanying the sp^2 hybridisation in the "clean" graphene domains.

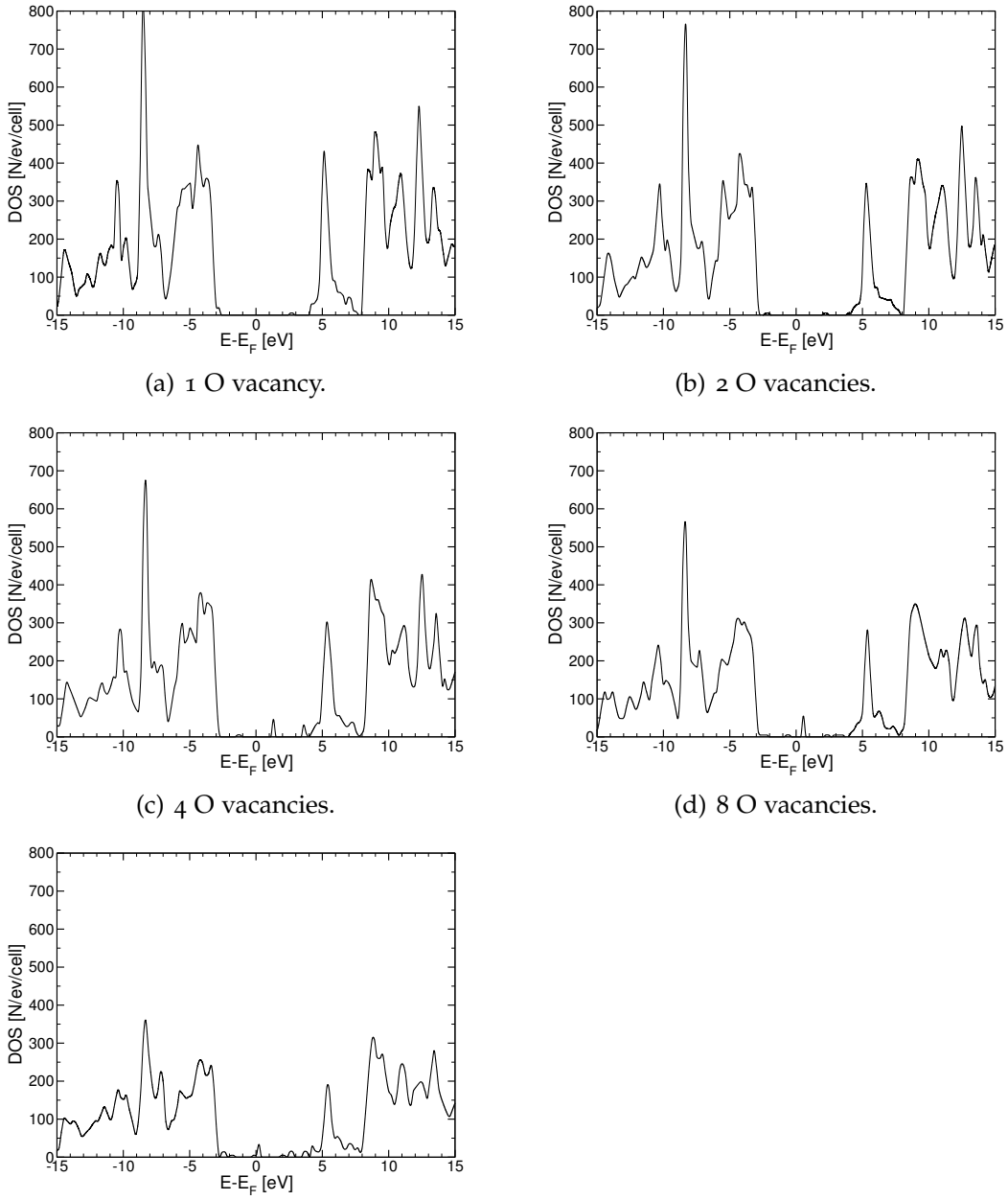

(a) 1 O vacancy.

(b) 2 O vacancies.

(c) 4 O vacancies.

(d) 8 O vacancies.

(e) 12 O vacancies.

Figure 5.14.: Density of states calculated using the PBE0 functional. States attributed to π bonds are seen to emerge in the $\sigma - \sigma^*$ gap, increasing with the number of O vacancies.

The density of states within the σ-σ^* gap is naturally low, given the small number of atoms contributing states. Indeed, for 1 O vacancy, Fig. 5.14(a) and 2 O vacancies, Fig. 5.14(b), the π states are barely noticeable on this scale. However, it is clearly these π states to which the narrowing of the energy gap can be attributed. Along side the decrease in the size of the π-π^* gap as the level of O coverage is reduced is a substantial increase in the density of states in the vicinity of the gap. This is more easily observed in the energy level plot depicted in Fig. 5.15. There is also a concomitant decrease in the density of states around the σ and σ^* levels. This is also in close agreement with experimental observations and supports the argument that these sp^2 domains are the origin of photoluminescence in rGO [100].

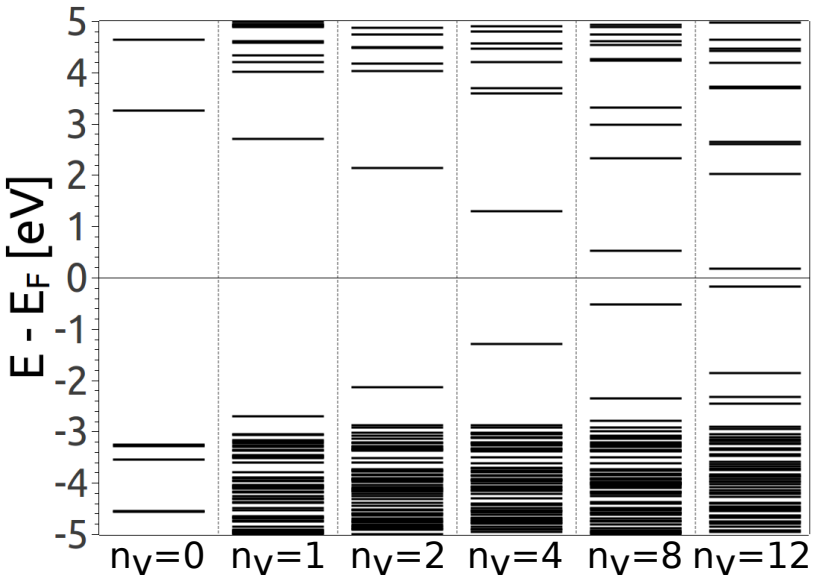

Figure 5.15.: Electron states of GO and rGO [173]. The $\pi - \pi^*$ gap is clearly seen to decrease with decreasing O coverage, while the $\sigma - \sigma^*$ gap remains relatively constant.

Visualisation of the Kohn Sham orbitals again helps to clarify this further. In Fig. 5.16 HOMO and LUMO are plotted with isosurfaces set to clearly

show π bonding and π^* anti-bonding orbitals. It can be seen that HOMO and LUMO are highly localised on the graphene islands, although the contribution of $2p_x$ and $2p_y$ states from some of the bordering O atoms is also visible. This localisation, or indeed confinement, of HOMO and LUMO to the sp^2 domains justifies the description of these regions as graphene quantum dots (GQD) [174].

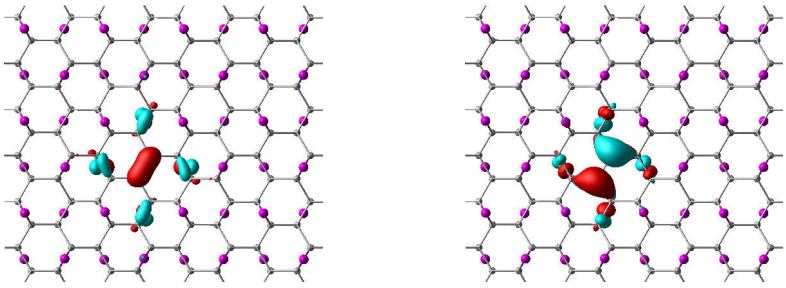

(a) HOMO: 1 O vacancy.

(b) LUMO: 1 O vacancy.

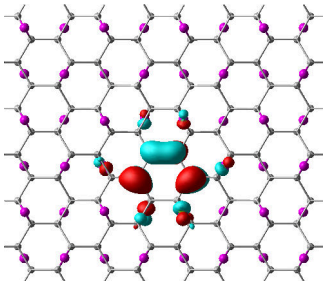

(c) HOMO: 2 O vacancies.

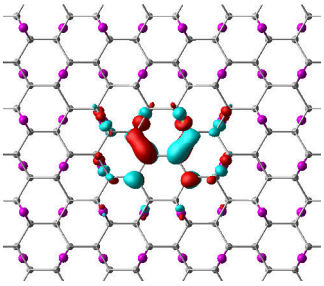

(d) LUMO: 2 O vacancies.

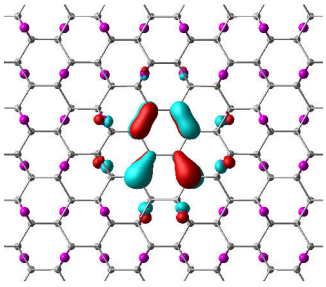

(e) HOMO: 4 O vacancies.

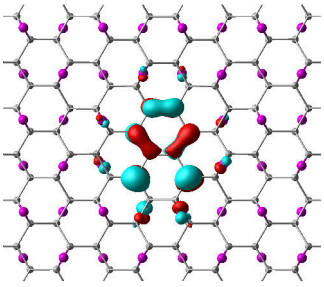

(f) LUMO: 4 O vacancies.

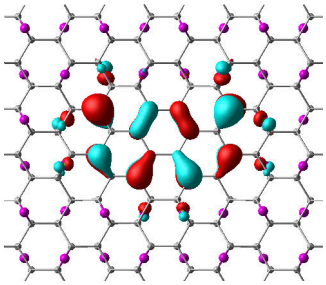

(g) HOMO: 8 O vacancies.

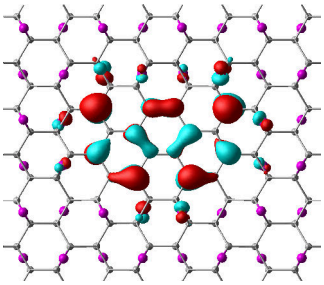

(h) LUMO: 8 O vacancies.

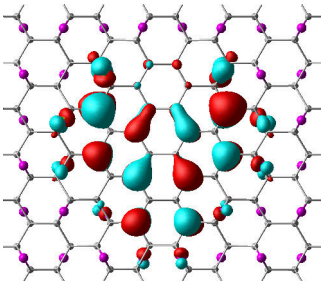

(i) HOMO: 12 O vacancies.

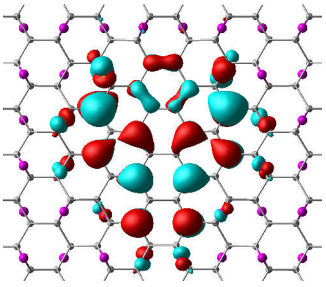

(j) LUMO: 12 O vacancies.

Figure 5.16.: Highest Occupied and Lowest Unoccupied Molecular Orbitals. Both HOMO and LUMO are seen to be localised on the graphene islands, while the distinct π orbitals evidence the local restoration of sp^2 hybridisation.

Effects of symmetry breaking

To investigate the effects of symmetry on the structural and electronics properties of rGO, simulations were performed on 8 different supercells with 4 O atoms removed. The structures are shown in Fig. 5.17, ordered from the most to the least thermodynamically stable. The structure already analysed in the preceding subsection is included in order to yield a better comparison. The binding energy per O atom and energy gap calculated using B3LYP and PBE0 is presented for each structure in Tab. 5.11. It is interesting to note that the two most stable structures are those of C_2^y point group symmetry. All other structures belong to the C_1 point group, possessing only translational symmetry by virtue of periodic boundary conditions.

Topology	E_c [eV]	E_g^{B3LYP} [eV]	E_g^{PBE0} [eV]
V_4^a	3.322	2.327	2.594
V_4^b	3.317	2.823	3.112
V_4^c	3.317	2.722	3.004
V_4^d	3.316	2.550	2.816
V_4^e	3.316	2.954	3.247
V_4^f	3.315	2.291	2.535
V_4^g	3.315	3.123	3.424
V_4^h	3.315	2.749	3.024

Table 5.11.: Binding energy per O atom and energy gaps of different symmetry arrangements for 4 O vacancies.

Immediately apparent is the range of energy gaps across the different structures, with the difference between the largest and smallest being $\sim$0.9 eV. The density of states is plotted for all structures in Fig. 5.18, from which it is clear that the σ-σ^* gap is once again relatively unaffected by the partial restoration of the sp^2 bonding network.

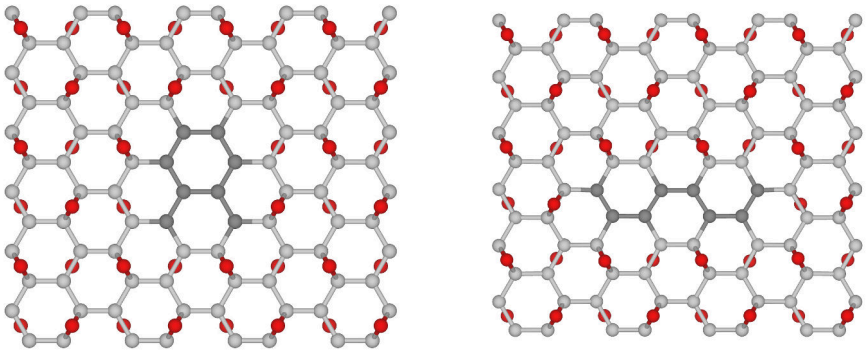

(a) V_4^a (b) V_4^b

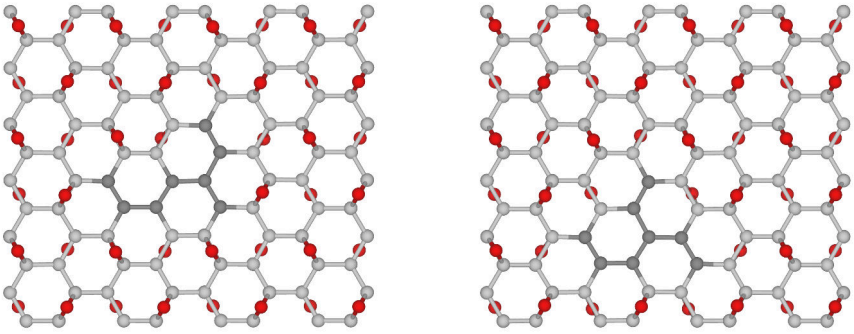

(c) V_4^c (d) V_4^d

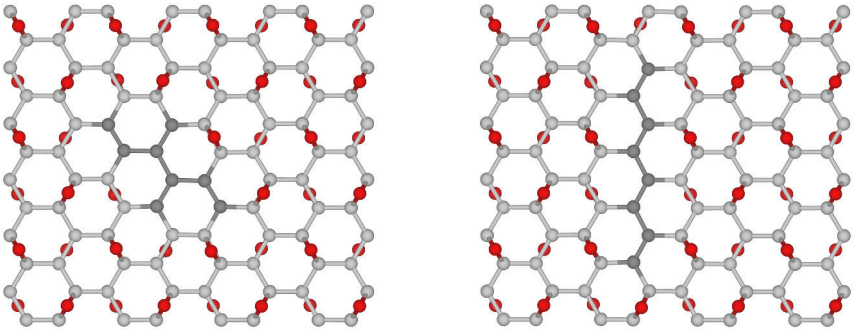

(e) V_4^e (f) V_4^f

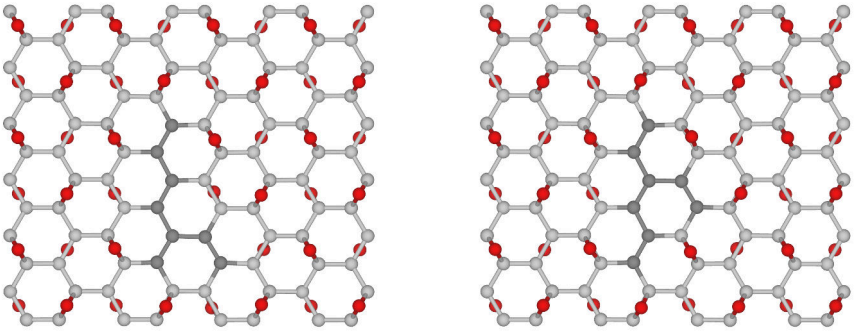

(g) V_4^g (h) V_4^h

Figure 5.17.: Different symmetry arrangements from the removal of 4 O atoms. C atoms not forming part of functional groups are again coloured darker for clarity.

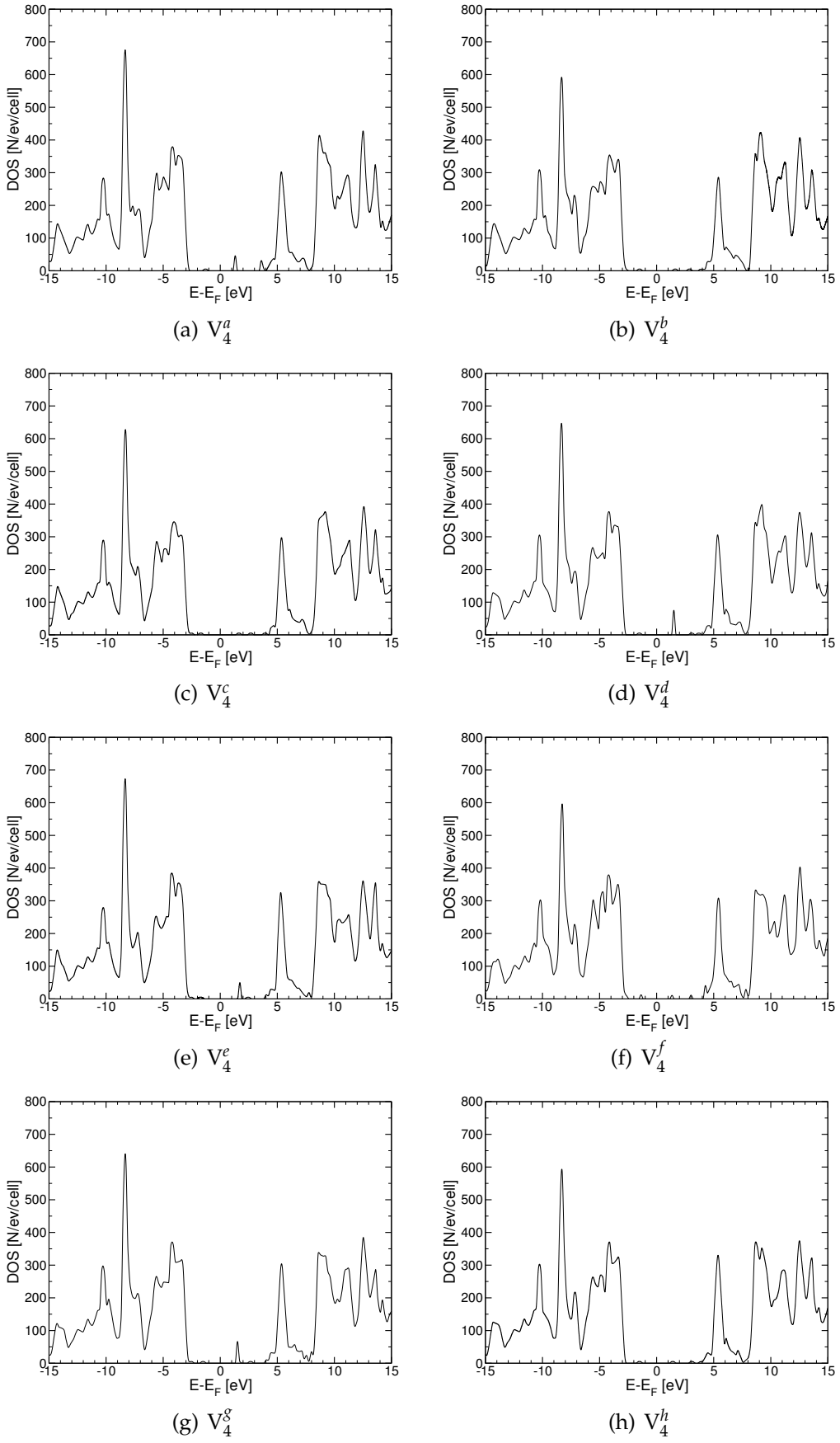

(a) V_4^a (b) V_4^b

(c) V_4^c (d) V_4^d

(e) V_4^e (f) V_4^f

(g) V_4^g (h) V_4^h

Figure 5.18.: Density of states (PBE0) for different symmetry arrangements of 4 O vacancies. The σ and σ^* states are again relatively unaffected, however there are marked differences within the $\sigma - \sigma^*$ gap.

This is yet another validification of the accuracy and applicability of the calculations presented here, as it agrees with experimental observations of quite uniform UV absorption across widely differing GO and rGO samples. It also helps to explain the observation of broad PL peaks [99] and sometimes seemingly inconsistent PL spectra [108]. As discussed before, chemically reduced GO is rather inhomogeneous and a range of sp^2 domains of differing size and shape can be expected to form. These will each be associated with unique π-π^* transitions as observed from these calculations, thereby contributing to PL across a range of wavelengths.

This also serves to highlight the importance of further development of precise "bottom-up" techniques for the production of GO with precisely tunable and consistent optical and electronic properties [175]. While there is no doubt that "top-down" synthesised GO and rGO are useful materials, the inherent limitations over the control of the topology of the sp^2 and functionalised domains will limit photonic device performance.

Absorption properties

The energy gaps predicted by the hybrid functionals run through the range of photon energies from the UV, through visible, to IR spectrum. The ability to tune the gap through this range is most advantageous for photonics applications if optical transitions are allowed [176]. In the same manner as for GO, the optical dipole matrix elements are calculated to determine whether or not this is the case. The dipole matrix elements for the structures of highest symmetry and greatest stability are presented in Tab. 5.12.

	PBE0			B3LYP		
n_{vac}	p_x[eV Å]	p_y[eV Å]	p_z[eV Å]	p_x[eV Å]	p_y[eV Å]	p_z[eV Å]
1	2.8015	3.0901	0.0002	2.6616	3.0505	0.0002
2	3.6151	0.0028	0.6729	3.3545	0.0026	0.6353
4	2.7778	0.0002	0.3659	2.5103	0.0001	0.3351
8	2.5758	0.0001	0.1261	2.1590	0.0001	0.1105
12	1.0026	0.0000	0.0211	0.7835	0.0000	0.0164

Table 5.12.: Dipole matrix elements of rGO.

All GQD structures can be seen to be optically active. All transitions allowed according to the point group symmetry of the structure are active. With the exception of the first structure with only one O atom removed, all share the C_2^y symmetry of their fully oxidised counterpart. Unlike GO, however, both x- and z- polarisations are active. The local symmetry in the vicinity of the O vacancy region for the structure with a single O vacancy is also of C_2 symmetry, but with the principle axis aligned along the z-direction. The C_2^z character table is provided for reference below.

For this point group, the irreducible representations allow transitions of either z- or both x- and y-polarisation, of which the latter is evident. To gain

	E	C_2^z	linear, rotations	quadratic
A	1	1	z, R_z	x^2, y^2, z^2, xy
B	1	-1	x, y, R_x, R_y	yz, xz

Table 5.13.: C_2^z character table.

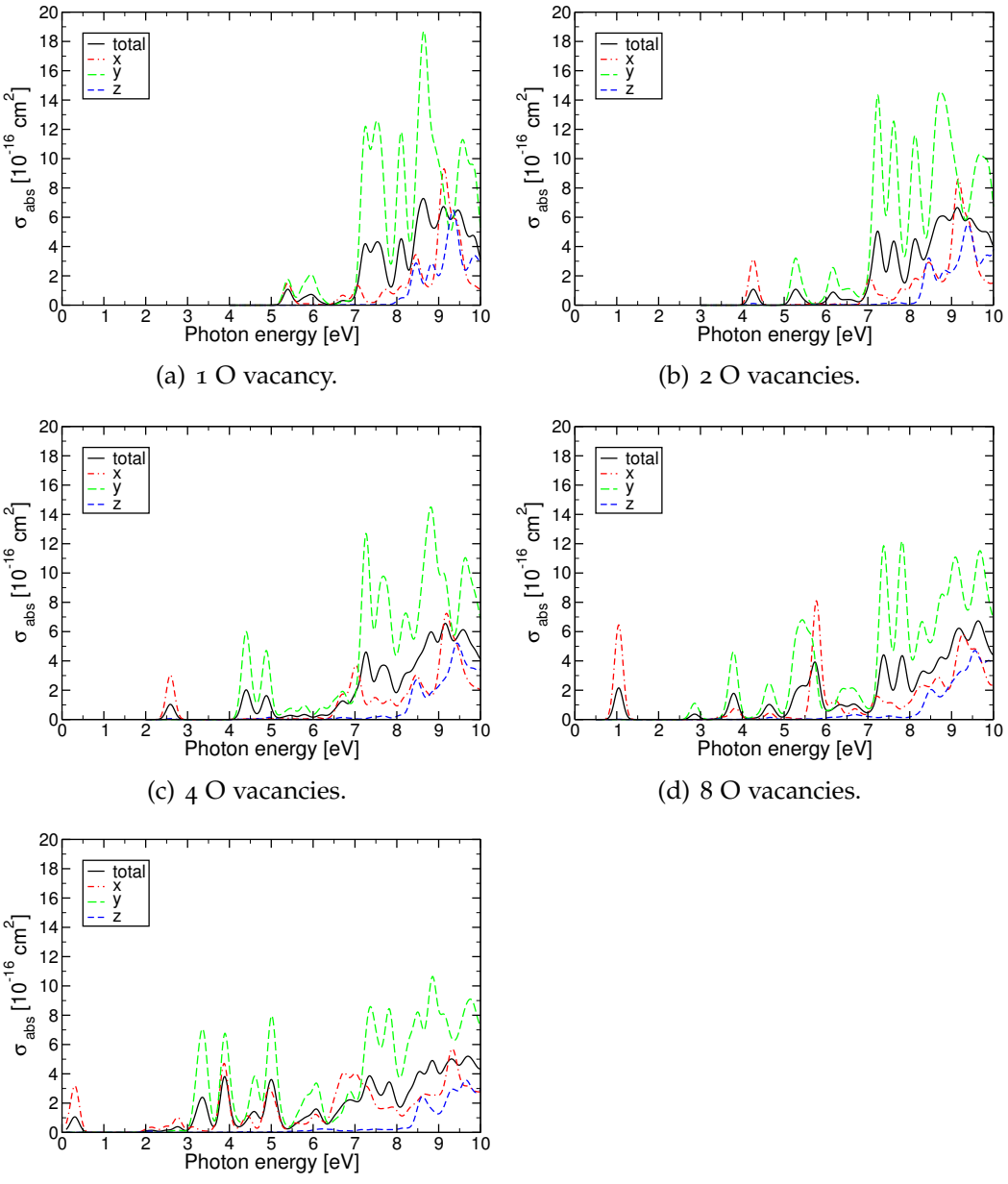

(a) 1 O vacancy.

(b) 2 O vacancies.

(c) 4 O vacancies.

(d) 8 O vacancies.

(e) 12 O vacancies.

Figure 5.19.: Absorption cross sections (PBE0), calculated using Eq. 4.7. Strong UV absorption is evident in all structures, while absorption peaks at the $\pi - \pi^*$ gap can be seen to redshift with decreasing O coverage.

further insight into the optical activity of rGO, the absorption cross section for each structure is calculated, as shown in Fig. 5.19. Strong absorption of UV light is apparent in all structures, while peaks associated with transitions at the fundamental gap are seen to move towards the visible and finally IR parts of the spectrum. Although all structures with 2 or more O vacancies have allowed p_z transitions at the HOMO-LUMO gap, absorption here is seen to be very weak, with p_x dominating. In all cases, z-polarised absorption only becomes clearly noticeable at higher (UV) photon energies. Beyond the gap, p_y absorption is dominant, again in all cases.

n_{vac}	τ_{if}^{rad} (PBE0) [ns]	τ_{if}^{rad} (B3LYP) [ns]
0	11.40	13.52
1	29.40	33.52
2	48.02	60.49
4	135.97	185.54
8	394.05	605.84
12	8138.31	17547.80

Table 5.14.: Radiative transition times of GO and rGO.

Radiative transition times for the structures of highest symmetry are presented in Tab. 5.14. The trend of increasing radiative times with the decrease of O coverage is to be expected [173]. Radiative lifetimes are inverse proportional to the modulus squared of the relevant dipole matrix element (see Eq. 4.6). The dipole matrix elements decrease in magnitude along with the energy gap, thereby explaining this behaviour. The radiative lifetime for the structure with 8 O vacancies, which has an energy gap of $\sim$1 eV, is approximately two orders of magnitude greater than for inorganic semiconductor QDs with a similar gap. The long radiative times are highly desirable for photovoltaic applications. Indeed long radiative times on the

order of μs, as with the structure with 12 O vacancies, have been measured in polymer solar cells using GO in carrier transport layers [119].

Inclusion of hydroxyl functional groups

Finally, in order to investigate the effects of the inclusion of hydroxyl functional groups on the electron and optical properties of rGO,[1] three structures chosen to be representative were modified and calculations were repeated in the same manner as previously. Adsorbates were again distributed evenly above and below the graphene sublattice in order to minimise Coulomb repulsion and maintain structural stability. This was achieved by removing epoxy moieties in pairs and replacing each with two hydroxyl groups, as shown in Fig. 5.20. Two of the supercells were formed in order to preserve the point group symmetry (Figs. 5.20(a) and 5.20(c)), while the symmetry is deliberately broken in the third (Fig. 5.20(b)).

Topology:	V_{OH}^{4a}	V_{OH}^{4b}	V_{OH}^{8}
n_{vac}	4	4	8
E_g^{B3LYP} [eV]	2.364	1.814	0.900
p_x [eV Å]	2.536	0	0.336
p_y [eV Å]	0.327	0.160	0.165
p_z [eV Å]	2.248	0	0.124
E_g^{PBE0} [eV]	2.630	2.209	1.050
p_x [eV Å]	2.803	0	0.368
p_y [eV Å]	0.424	0.140	0.187
p_z [eV Å]	2.571	0	0.142

Table 5.15.: Energy gaps and dipole matrix elements for OH containing structures.

As can be seen by comparing the energy gaps for structures including hydroxyl moieties in Tab. 5.15 with those for the corresponding purely

1 Given that carbonyl and carboxyl moieties are known to form on the edges of GO flakes, the use of periodic boundary conditions precludes the study of these.

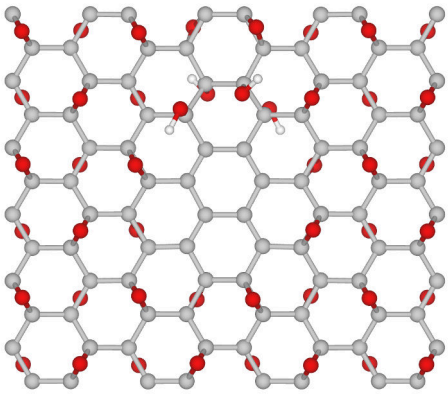

(a) V_{OH}^{4a}.

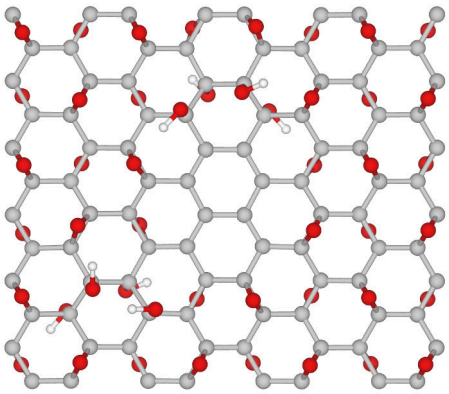

(b) V_{OH}^{4b}.

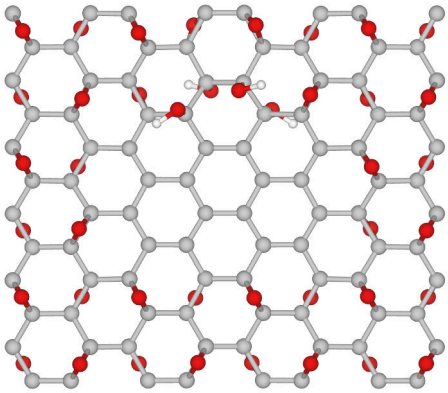

(c) V_{OH}^{8}.

Figure 5.20.: Quantum dot structures with hydroxyl functional groups. Epoxy groups are replaced with pairs of hydroxyl groups. The C_2^y symmetry of the purely epoxy functionalised structure is deliberately broken in (b).

epoxy functionalised structures in Tab. 5.10, the presence of these functional groups does not significantly affect the electronic structure. Indeed, the difference in energy gaps between the corresponding structures with preserved symmetry is almost negligible. For 4 O vacancies, the difference in the PBE0 energy gap is 36 meV, while for 8 O vacancies it is a mere 6 meV. The difference in dipole matrix elements is similarly very small. Of much greater significance is the disruption of symmetry, in which case the difference between the PBE0 energy gaps is 0.385 eV. The removal of symmetry also means that all dipole transitions are optically allowed.

This serves as a final confirmation that the choice of a purely epoxy functionalised model of GO and rGO is representative of the real material. Moreover, it adds weight to the conclusion drawn at the end of section 5.4.2 that the electronic and optical properties of rGO are strongly influenced by the symmetry of the sp^2 and functionalised domains.

6

CONCLUSIONS

SUMMARY OF FINDINGS

A detailed review of the literature, presented in chapter 2, revealed that graphene oxide (GO) and reduced graphene oxide (rGO) possess many fascinating and useful electronic and optical properties that make them promising materials for photonics applications. Of particular value to this end is the fact that these properties are highly tunable by manipulation of the bonding. This can be done by oxidisation of graphene to create sp^3 hybridised domains, thus disrupting the π bonding network responsible for graphene's electronic properties. Conversely, GO can be reduced to form sp^2 domains within the wider sp^3 matrix.

A considerable amount of research has been focused on attempting to understand the mechanisms involved in the oxidisation of graphene and reduction of GO, the exact nature of the optical and electronic properties, and the exploitation of these in the design and production of photovoltaic cells, photocatalysts. optical sensors, and even targeted cancer drugs.

Yet, there is still debate over such fundamental issues as to what actually constitutes GO and rGO and the origin of and mechanisms for photolumi-

nescence (PL), for example. Theoretical and computational studies have an important role to play in the ultimate understanding of these matters. Indeed, many studies based on density functional theory (DFT) simulations and other theoretical techniques have been conducted and published in this regard. However, most existing DFT studies of the optical and electronic properties of GO and rGO are limited by the failure of DFT to accurately predict the energy gap, the most important factor for this.

Therefore, in an effort to gain a finer insight into these properties, a detailed study of rGO based on hybrid DFT has been carried out. It has been demonstrated by means of a small comparative study of the predictive capabilities of *ab initio* and hybrid DFT in the calculation of the energy gaps of well-known III-V semiconductors that the latter is a powerful tool for this purpose.

Using an epoxy functionalised model of GO, quantitative prediction of the energy gap at varying levels of reduction has been made. From the B3LYP calculations, the band gap of fully sp^3 hybridised GO is predicted as 6.5 eV. This agrees almost perfectly with experimental measurements of the σ-σ^* transition of GO, which is responsible for the observed strong UV absorption. Upon removal of O atoms from a GO supercell, the σ-σ^* gap is shown to remain relatively static, in further agreement with experimental observations. The associated decrease of the energy gap is shown to originate from the emergence of C π and π^* states inside the σ-σ^* gap.

Calculations of the dipole matrix elements of GO confirm that the fundamental gap is optically active and polarisation selective. The principal components of the dielectric constant, $\epsilon_{xx} = 1.291$, $\epsilon_{yy} = 1.387$, and $\epsilon_{zz} = 1.087$ (again from B3LYP) show GO to be optically anisotropic, which is an intrinsic property of 2D materials.

For rGO structures in which the symmetry of GO is maintained and the removal of O atoms forms "islands" of sp^2 conjugated carbon, the evolution of the energy gap is shown to fit an exceptionally simple relationship, $E_g(n_{vac}) = E_g^0 \exp[-0.25 n_{vac}]$, where E_g^0 is the band gap of GO and n_{vac} is the number of O atoms removed from the supercell. This suggests that the energy gap of GO can be tuned from the range of UV, through visible and down to infrared light. This is in line with observations from UV-visible spectroscopy of the red-shift of absorption peaks during the reduction of GO.

An inspection of the highest occupied (HOMO) and lowest unoccupied (LUMO) molecular orbitals in these structures shows them to be highly localised to the graphene domains. The restoration of sp^2 bonding is evidenced by the characteristic π bonds. This suggests that these domains may be described as graphene quantum dots (GQDs) embedded in a GO super-lattice.

An exploration of the effect of symmetry breaking on the energy gap predicts a wide range, across 0.9 eV, of gaps from structures with the same number of epoxy functional groups. This suggests an explanation for the observation of broad PL peaks from samples of chemically reduced GO, in that PL emission likely originates from multiple sp^2 domains of varying shape and size and hence different π-π^* gaps. This prediction also poses a challenge for the production of GO and rGO with consistent properties.

Calculated absorption cross-sections for the GQD structures show rGO to be dichroic and predict strong absorption in the UV range along with polarisation-selective absorption at the π-π^* gap. Long radiative lifetimes are predicted, which are of great importance to achieve carrier separation in photovoltaic devices.

The addition of hydroxyl moieties to three supercells confirms that the electronic structure of rGO is dominated by epoxy groups. Comparing calculated energy gaps from the related structures with and without hydroxyl groups show little difference when the symmetry is not modified. In the case where symmetry was deliberately broken, a significant change of $\sim$0.5 eV is caused. This falls in line with the other calculations where the symmetry has been reduced. This result provides further justification for the use of a purely epoxy functionalised model of GO and reiterates the importance of symmetry in the manipulation of the optical properties of rGO.

FURTHER WORK AND EVALUATION OF METHODOLOGY

Although the results and analysis presented offer substantial insight into the optical properties of GO and rGO and aid in the explanation of many experimental observations, there are some limitations of the methodology employed. For example the structure adopted is an ideal one, whereas experiments are typically carried out on GO and rGO flakes in suspension or sheets and membranes on a substrate. In the latter case, the orbitals from the substrate can contribute to the sp^3 hybridised bonds. It would therefore be interesting to repeat some of these calculations for a sheet of GO on an SiC [111] surface, or similar, to simulate how this affects the optical properties.

It would also be of interest to recalculate the adsorption energies using dispersion corrections, such as Grimme's methods [177]. This was not initially considered as the O adatoms are chemisorbed rather than physisorbed to the surface. It would be useful to quantify this, however.

An additional limitation of the study is the size of the supercell used. The largest embedded GQD was formed by the removal of 12 O atoms. Calculations with 16 O atoms proved to be impossible to converge, almost certainly owing to spurious interactions as a result of the supercell being too small. Resource limitations prevented larger calculations being performed, however with the current availability of a larger HPC cluster it would be most interesting to determine at which point the system undergoes transition to a conducting state.

Finally, in comparison to when this study was started, the size of systems that can simulated using the GW approximation has increased considerably. Although comparison to experiment suggests that the B3LYP calculated energy gaps are accurate, it would be of great benefit to repeat some of the calculations at this level of theory for comparison. This would also facilitate the study of excitons in the GQDs.

REFERENCES

[1] K. Novoselov et al. "Electric field effect in atomically thin carbon films". In: *Science* 306 (2004), pp. 666–669.

[2] A. K. Geim and K. S. Novoselov. "The rise of graphene". In: *Nat. Mater.* 6 (2007), pp. 183–191.

[3] K. S. Novoselov et al. "Two-dimensional gas of massless Dirac fermions in graphene". In: *Nature* 438 (2005), pp. 197–200.

[4] A. A. Balandin et al. "Superior Thermal Conductivity of Single-Layer Graphene". In: *Nano Lett.* 8 (2008), pp. 902–907.

[5] R. R. Nair et al. "Fine Structure Constant Defines Visual Transparency of Graphene". In: *Science* 320 (2008), pp. 1308–1308.

[6] F. Bonaccorso et al. "Graphene photonics and optoelectronics". In: *Nat. Photon.* 4 (2010), pp. 611–622.

[7] D. Li et al. "Processable aqueous dispersions of graphene nanosheets". In: *Nat. Nano.* 3 (2008), pp. 101–105.

[8] L. A. Ponomarenko et al. "Chaotic Dirac Billiard in Graphene Quantum Dots". In: *Science* 320 (2008), pp. 356–358.

[9] V. Georgakilas et al. "Functionalization of Graphene: Covalent and Non-Covalent Approaches, Derivatives and Applications". In: *Chem. Rev.* 112 (2012), pp. 6156–6214.

[10] T. Kuila et al. "Chemical functionalization of graphene and its applications". In: *Prog. Mater. Sci.* 57 (2012), pp. 1061–1105.

[11] X. Jiang et al. "Graphene oxide as a chemically tunable 2-D material for visible-light photocatalyst applications". In: *J. Catal.* 299 (2013), pp. 204–209.

[12] T.-F. Yeh et al. "Roles of graphene oxide in photocatalytic water splitting". In: *Mater. Today* 16 (2013), pp. 78–84.

[13] H.-C. Hsu et al. "Graphene oxide as a promising photocatalyst for CO2 to methanol conversion". In: *Nanoscale* 5 (1 2013), pp. 262–268.

[14] L. J. Larsen et al. “Optimization and Doping of Reduced Graphene Oxide-Silicon Solar Cells”. In: *J. Phys. Chem. C* (2015),

[15] M. Wang et al. “All-Solid-State Reduced Graphene Oxide Supercapacitor with Large Volumetric Capacitance and Ultralong Stability Prepared by Electrophoretic Deposition Method”. In: *ACS Appl. Mater. Interfaces* 7.2 (2015), pp. 1348–1354.

[16] G. Gonçalves et al. “Breakdown into nanoscale of graphene oxide: Confined hot spot atomic reduction and fragmentation”. In: *Sci. Rep.* 4 (2014), pp. 6735–.

[17] K. Lejaeghere et al. “Reproducibility in density functional theory calculations of solids”. In: *Science* 351 (2016), aad3000.

[18] J. Heyd et al. “Energy band gaps and lattice parameters evaluated with the Heyd-Scuseria-Ernzerhof screened hybrid functional”. In: *J. Chem. Phys.* 123, 174101 (2005), p. 174101.

[19] S. Tomić, B. Montanari, and N. M. Harrison. “The group III-V’s semiconductor energy gaps predicted using the B3LYP hybrid functional”. In: *Physica E* 40 (2008), pp. 2125–2127.

[20] P. R. Wallace. “The Band Theory of Graphite”. In: *Phys. Rev.* 71 (1947), pp. 622–634.

[21] H. Boehm, R. Setton, and E. Stumpp. “Nomenclature and terminology of graphite intercalation compounds”. In: *Carbon* 24 (1986), pp. 241–245.

[22] C. Lee et al. “Measurement of the Elastic Properties and Intrinsic Strength of Monolayer Graphene”. In: *Science* 321 (2008), pp. 385–388.

[23] J.-U. Lee, D. Yoon, and H. Cheong. “Estimation of Young’s Modulus of Graphene by Raman Spectroscopy”. In: *Nano Lett.* 12 (2012), pp. 4444–4448.

[24] A. H. Castro Neto et al. “The electronic properties of graphene”. In: *Rev. Mod. Phys.* 81 (2009), pp. 109–162.

[25] M. Pumera and C. H. A. Wong. “Graphane and hydrogenated graphene”. In: *Chem. Soc. Rev.* 42 (2013), pp. 5987–5995.

[26] M. H. F. Sluiter and Y. Kawazoe. "Cluster expansion method for adsorption: Application to hydrogen chemisorption on graphene". In: *Phys. Rev. B* 68 (2003), p. 085410.

[27] J. O. Sofo, A. S. Chaudhari, and G. D. Barber. "Graphane: A two-dimensional hydrocarbon". In: *Phys. Rev. B* 75 (2007), p. 153401.

[28] L. Hornekær et al. "Metastable Structures and Recombination Pathways for Atomic Hydrogen on the Graphite (0001) Surface". In: *Phys. Rev. Lett.* 96 (2006), p. 156104.

[29] R. Balog et al. "Atomic Hydrogen Adsorbate Structures on Graphene". In: *J. Am. Chem. Soc.* 131 (2009), pp. 8744–8745.

[30] R. Balog et al. "Bandgap opening in graphene induced by patterned hydrogen adsorption". English. In: *Nat. Mater.* 9 (2010), pp. 315–319.

[31] J. Zhou et al. "Tuning electronic and magnetic properties of graphene by surface modification". In: *Appl. Phys. Lett.* 95, 103108 (2009),

[32] R. R. Nair et al. "Fluorographene: A Two-Dimensional Counterpart of Teflon". In: *Small* 6 (2010), pp. 2877–2884.

[33] S. Stankovich et al. "Graphene-based composite materials". In: *Nature* 442 (2006), pp. 282–286.

[34] S. Sarkar, E. Bekyarova, and R. C. Haddon. "Covalent chemistry in graphene electronics". In: *Mater. Today* 15 (2012), pp. 276–285.

[35] B. C. Brodie. "On the Atomic Weight of Graphite". In: *Phil. Trans. R. Soc. Lond.* 149 (1859), pp. 249–259.

[36] W. S. Hummers and R. E. Offeman. "Preparation Of Graphitic Oxide". In: *J. Am. Chem. Soc.* 80 (1958), p. 1339.

[37] D. C. Marcano et al. "Improved Synthesis of Graphene Oxide". In: *ACS Nano* 4 (2010), pp. 4806–4814.

[38] D. He et al. "Mechanism of a green graphene oxide reduction with reusable potassium carbonate". In: *RSC Adv.* 5 (2015), pp. 11966–11972.

[39] S. Park and R. S. Ruoff. "Chemical methods for the production of graphenes". In: *Nat. Nano.* 4 (2009), pp. 217–224.

[40] H. Wang and Y. H. Hu. "Effect of Oxygen Content on Structures of Graphite Oxides". In: *Ind. Eng. Chem. Res.* 50 (2011), pp. 6132–6137.

[41] S. Stankovich et al. “Synthesis and exfoliation of isocyanate-treated graphene oxide nanoplatelets”. In: *Carbon* 44 (2006), pp. 3342–3347.

[42] W. Cai et al. “Synthesis and Solid-State NMR Structural Characterization of 13C-Labeled Graphite Oxide”. In: *Science* 321 (2008), pp. 1815–1817.

[43] W. Gao et al. “New insights into the structure and reduction of graphite oxide”. In: *Nat. Chem.* 1 (2009), pp. 403–408.

[44] V. C. Tung et al. “High-throughput solution processing of large-scale graphene”. In: *Nat. Nano.* 4 (2009), pp. 25–29.

[45] A. Bagri et al. “Structural evolution during the reduction of chemically derived graphene oxide”. In: *Nat. Chem.* 2 (2010), 581–587.

[46] K. Erickson et al. “Determination of the Local Chemical Structure of Graphene Oxide and Reduced Graphene Oxide”. In: *Adv. Mater.* 22 (2010), pp. 4467–4472.

[47] X. Gao, J. Jang, and S. Nagase. “Hydrazine and Thermal Reduction of Graphene Oxide: Reaction Mechanisms, Product Structures, and Reaction Design”. In: *J. Phys. Chem. C* 114 (2010), pp. 832–842.

[48] C. K. Chua and M. Pumera. “The reduction of graphene oxide with hydrazine: elucidating its reductive capability based on a reaction-model approach”. In: *Chem. Commun.* 52 (2016), pp. 72–75.

[49] S. Eigler and A. Hirsch. “Chemistry with Graphene and Graphene Oxide - Challenges for Synthetic Chemists”. In: *Angew. Chem. Int. Ed. Engl.* 53 (2014), pp. 7720–7738.

[50] D. A. Dikin et al. “Preparation and characterization of graphene oxide paper”. In: *Nature* 448 (2007), pp. 457–460.

[51] V. Chandra et al. “Water-Dispersible Magnetite-Reduced Graphene Oxide Composites for Arsenic Removal”. In: *ACS Nano* 4 (2010), pp. 3979–3986.

[52] O. C. Compton and S. T. Nguyen. “Graphene Oxide, Highly Reduced Graphene Oxide, and Graphene: Versatile Building Blocks for Carbon-Based Materials”. In: *Small* 6 (2010), pp. 711–723.

[53] Y. Zhu et al. “Graphene and Graphene Oxide: Synthesis, Properties, and Applications”. In: *Adv. Mater.* 22 (2010), pp. 3906–3924.

[54] G. Ceriotti et al. “Rapid method for the purification of graphene oxide”. In: *RSC Adv.* 5 (2015), pp. 50365–50371.

[55] K. P. Loh et al. “Graphene oxide as a chemically tunable platform for optical applications”. In: *Nat. Chem.* 2 (2010), pp. 1015–1024.

[56] D. Chen, H. Feng, and J. Li. “Graphene Oxide: Preparation, Functionalization, and Electrochemical Applications”. In: *Chem. Rev.* 112 (2012), pp. 6027–6053.

[57] D. R. Dreyer et al. “The chemistry of graphene oxide”. In: *Chem. Soc. Rev.* 39 (2010), pp. 228–240.

[58] C. Gómez-Navarro et al. “Atomic Structure of Reduced Graphene Oxide”. In: *Nano Lett.* 10 (2010), pp. 1144–1148.

[59] A. Barinov et al. “Initial Stages of Oxidation on Graphitic Surfaces: Photoemission Study and Density Functional Theory Calculations”. In: *J. Phys. Chem. C* 113 (2009), pp. 9009–9013.

[60] N. Ghaderi and M. Peressi. “First-Principle Study of Hydroxyl Functional Groups on Pristine, Defected Graphene, and Graphene Epoxide”. In: *J. Phys. Chem. C* 114 (2010), pp. 21625–21630.

[61] T. Szabó et al. “Evolution of Surface Functional Groups in a Series of Progressively Oxidized Graphite Oxides”. In: *Chem. Mater.* 18 (2006), pp. 2740–2749.

[62] U. Hofmann and R. Holst. “Über die Säurenatur und die Methylierung von Graphitoxyd”. In: *Ber. Dtsch. Chem. Ges.* 72 (1939), pp. 754–771.

[63] G. Ruess. “Über das Graphitoxyhydroxyd (Graphitoxyd)”. In: *Monatsh. Chem. Verw. Tl.* 76 (1946), pp. 381–417.

[64] R. J. W. E. Lahaye et al. “Density functional theory study of graphite oxide for different oxidation levels”. In: *Phys. Rev. B* 79 (2009), p. 125435.

[65] W. Scholz and H. P. Boehm. “Untersuchungen am Graphitoxid. VI. Betrachtungen zur Struktur des Graphitoxids”. In: *Z. Anorg. Allg. Chem.* 369 (1969), pp. 327–340.

[66] T. Nakajima, A. Mabuchi, and R. Hagiwara. “A new structure model of graphite oxide”. In: *Carbon* 26 (1988), pp. 357–361.

[67] T. Nakajima and Y. Matsuo. “Formation process and structure of graphite oxide”. In: *Carbon* 32 (1994), pp. 469–475.

[68] S. Mao, H. Pu, and J. Chen. "Graphene oxide and its reduction: modeling and experimental progress". In: *RSC Adv.* 2 (2012), pp. 2643–2662.

[69] H. He et al. "A new structural model for graphite oxide". In: *Chem. Phys. Lett.* 287 (1998), pp. 53–56.

[70] H. He et al. "Solid-State NMR Studies of the Structure of Graphite Oxide". In: *J. Phys. Chem.* 100 (1996), pp. 19954–19958.

[71] A. Lerf et al. "13C and 1H MAS NMR studies of graphite oxide and its chemically modified derivatives". In: *Solid State Ion.* 101-103, Part 2 (1997), pp. 857–862.

[72] A. Lerf et al. "Structure of Graphite Oxide Revisited". In: *J. Phys. Chem. B* 102 (1998), pp. 4477–4482.

[73] M. J. McAllister et al. "Single Sheet Functionalized Graphene by Oxidation and Thermal Expansion of Graphite". In: *Chem. Mater.* 19 (2007), pp. 4396–4404.

[74] K. N. Kudin et al. "Raman Spectra of Graphite Oxide and Functionalized Graphene Sheets". In: *Nano Lett.* 8 (2008), pp. 36–41.

[75] H.-K. Jeong et al. "Evidence of Graphitic AB Stacking Order of Graphite Oxides". In: *J. Am. Chem. Soc.* 130 (2008), pp. 1362–1366.

[76] H.-K. Jeong et al. "X-ray absorption spectroscopy of graphite oxide". In: *EPL* 82 (2008), p. 67004.

[77] K. A. Mkhoyan et al. "Atomic and Electronic Structure of Graphene-Oxide". In: *Nano Lett.* 9 (2009), 1058–1063.

[78] D. Pacilé et al. "Electronic properties and atomic structure of graphene oxide membranes". In: *Carbon* 49 (2011), pp. 966–972.

[79] R. Larciprete et al. "Dual Path Mechanism in the Thermal Reduction of Graphene Oxide". In: *J. Am. Chem. Soc.* 133 (2011), pp. 17315–17321.

[80] L. Liu et al. "Graphene Oxidation: Thickness-Dependent Etching and Strong Chemical Doping". In: *Nano Lett.* 8 (2008), pp. 1965–1970.

[81] L. Liu et al. "Controlled oxidative functionalization of monolayer graphene by water-vapor plasma etching". In: *Carbon* 50 (2012), pp. 3039–3044.

[82] N. A. Vinogradov et al. “Impact of Atomic Oxygen on the Structure of Graphene Formed on Ir(111) and Pt(111)”. In: *J. Phys. Chem. C* 115 (2011), pp. 9568–9577.

[83] M. Z. Hossain et al. “Chemically homogeneous and thermally reversible oxidation of epitaxial graphene”. In: *Nat. Chem.* 4 (2012), pp. 305–309.

[84] X. Yu et al. “New synthesis method for the growth of epitaxial graphene”. In: *J. Electron Spectrosc. Relat. Phenom.* 184 (2011), pp. 100–106.

[85] J. Aumanen et al. “Patterning and tuning of electrical and optical properties of graphene by laser induced two-photon oxidation”. In: *Nanoscale* 7 (2015), pp. 2851–2855.

[86] D. W. Boukhvalov and M. I. Katsnelson. “Modeling of Graphite Oxide”. In: *J. Am. Chem. Soc.* 130 (2008), pp. 10697–10701.

[87] L. Wang et al. “Stability of graphene oxide phases from first-principles calculations”. In: *Phys. Rev. B* 82 (2010), p. 161406.

[88] J.-A. Yan, L. Xian, and M. Y. Chou. “Structural and Electronic Properties of Oxidized Graphene”. In: *Phys. Rev. Lett.* 103 (2009), p. 086802.

[89] M. Topsakal and S. Ciraci. “Domain formation on oxidized graphene”. English. In: *Phys. Rev. B* 86 (2012).

[90] H. Huang et al. “Oxygen density dependent band gap of reduced graphene oxide”. In: *J. Appl. Phys.* 111, 054317 (2012).

[91] S. Y. Zhou et al. “Substrate-induced bandgap opening in epitaxial graphene”. In: *Nat. Mater.* 6 (2007), pp. 770–775.

[92] R. Martinazzo, S. Casolo, and G. F. Tantardini. “Symmetry-induced band-gap opening in graphene superlattices”. In: *Phys. Rev. B* 81 (2010), p. 245420.

[93] R. Skomski et al. “Sublattice-induced symmetry breaking and band-gap formation in graphene”. In: *Mater. Horiz.* 1 (2014), pp. 563–571.

[94] K.-Y. Lian et al. “Big Bandgap in Highly Reduced Graphene Oxides”. In: *J. Phys. Chem. C* 117 (2013), pp. 6049–6054.

[95] Ž. Šljivančanin et al. "Binding of atomic oxygen on graphene from small epoxy clusters to a fully oxidized surface". In: *CARBON* 54 (2013), pp. 482–488.

[96] S. Niyogi et al. "Solution properties of graphite and graphene". English. In: *J. Am. Chem. Soc.* 128 (2006), pp. 7720–7721.

[97] X. Sun et al. "Nano-Graphene Oxide for Cellular Imaging and Drug Delivery". In: *Nano Res.* 1 (2008), pp. 203–212.

[98] Z. Liu et al. "PEGylated Nanographene Oxide for Delivery of Water-Insoluble Cancer Drugs". In: *J. Am. Chem. Soc.* 130 (2008), pp. 10876–10877.

[99] Z. Luo et al. "Photoluminescence and band gap modulation in graphene oxide". In: *Appl. Phys. Lett.* 94, 111909 (2009).

[100] G. Eda et al. "Blue Photoluminescence from Chemically Derived Graphene Oxide". In: *Adv. Mater.* 22 (2010), p. 505.

[101] Y. Shen et al. "Optical investigation of reduced graphene oxide by spectroscopic ellipsometry and the band-gap tuning". In: *Appl. Phys. Lett.* 99, 141911 (2011), p. 141911.

[102] Y. Shen et al. "Evolution of the band-gap and optical properties of graphene oxide with controllable reduction level". In: *Carbon* 62 (2013), pp. 157–164.

[103] A. Mathkar et al. "Controlled, Stepwise Reduction and Band Gap Manipulation of Graphene Oxide". In: *J. Phys. Chem. Lett.* 3 (2012), pp. 986–991.

[104] D. Lee et al. "Quantum confinement-induced tunable exciton states in graphene oxide". In: *Sci. Rep.* 3 (2013).

[105] F. Liu et al. "Facile Synthetic Method for Pristine Graphene Quantum Dots and Graphene Oxide Quantum Dots: Origin of Blue and Green Luminescence". In: *Adv. Mater.* 25 (2013), pp. 3657–3662.

[106] M.-H. Jang et al. "Is the Chain of Oxidation and Reduction Process Reversible in Luminescent Graphene Quantum Dots?" In: *Small* 11 (2015), pp. 3773–3781.

[107] H. F. Liang et al. “The band structure of graphene oxide examined using photoluminescence spectroscopy”. In: *J. Mater. Chem. C* 3 (2015), pp. 12484–12491.

[108] S. K. Pal. “Versatile photoluminescence from graphene and its derivatives”. In: *Carbon* 88 (2015), pp. 86–112.

[109] T.-F. Yeh et al. “Graphene oxide-based nanomaterials for efficient photoenergy conversion”. In: *J. Mater. Chem. A* 4 (2016), pp. 2014–2048.

[110] E. Singh and H. S. Nalwa. “Stability of graphene-based heterojunction solar cells”. In: *RSC Adv.* 5 (2015), pp. 73575–73600.

[111] X. Wan et al. “Graphene - A Promising Material for Organic Photovoltaic Cells”. In: *Adv. Mater.* 23 (2011), pp. 5342–5358.

[112] Z. Yin et al. “Organic Photovoltaic Devices Using Highly Flexible Reduced Graphene Oxide Films as Transparent Electrodes”. In: *ACS Nano* 4 (2010), pp. 5263–5268.

[113] J. Wu et al. “Organic solar cells with solution-processed graphene transparent electrodes”. In: *Appl. Phys. Lett.* 92 (2008).

[114] Y. Xu et al. “Polymer photovoltaic devices with transparent graphene electrodes produced by spin-casting”. In: *Carbon* 48 (2010), pp. 3308–3311.

[115] M.-H. Yeh et al. “Dye-Sensitized Solar Cells with Reduced Graphene Oxide as the Counter Electrode Prepared by a Green Photothermal Reduction Process”. In: *ChemPhysChem* 15 (2014), pp. 1175–1181.

[116] C. Petridis et al. “Solution processed reduced graphene oxide electrodes for organic photovoltaics”. In: *Nanoscale Horiz.* (2016),

[117] S.-S. Li et al. “Solution-Processable Graphene Oxide as an Efficient Hole Transport Layer in Polymer Solar Cells”. In: *ACS Nano* 4 (2010), pp. 3169–3174.

[118] A. Iwan and A. Chuchmala. “Perspectives of applied graphene: Polymer solar cells”. In: *Prog. Polym. Sci.* 37 (2012), pp. 1805–1828.

[119] J. Liu, M. Durstock, and L. Dai. “Graphene oxide derivatives as hole- and electron-extraction layers for high-performance polymer solar cells”. In: *Energy Environ. Sci.* 7 (2014), pp. 1297–1306.

[120] C. T. G. Smith et al. “Graphene oxide hole transport layers for large area, high efficiency organic solar cells”. In: *Appl. Phys. Lett.* 7 (2014).

[121] J. Liu et al. “Graphene Oxide Nanoribbon as Hole Extraction Layer to Enhance Efficiency and Stability of Polymer Solar Cells”. In: *Adv. Mater.* 26 (2014), pp. 786–790.

[122] K. D. G. I. Jayawardena et al. “Solution processed reduced graphene oxide/metal oxide hybrid electron transport layers for highly efficient polymer solar cells”. In: *J. Mater. Chem. A* 1 (2013), pp. 9922–9927.

[123] H. Woo Lee et al. “Highly efficient inverted polymer solar cells with reduced graphene-oxide-zinc-oxide nanocomposites buffer layer”. In: *Appl. Phys. Lett.* 102 (2013).

[124] E. Kaxiras. *Atomic and Electronic Structure of Solids*. Cambridge University Press, 2003.

[125] R. M. Martin. *Electronic Structure: Basic Theory and Practical Methods*. Cambridge University Press, 2011.

[126] R. G. Parr and W. Yang. *Density-Functional Theory of Atoms and Molecules*. Oxford University Press, 1989.

[127] J. C. Slater. “The Theory of Complex Spectra”. In: *Phys. Rev.* 34 (1929), pp. 1293–1322.

[128] C. C. J. Roothaan. “New Developments in Molecular Orbital Theory”. In: *Rev. Mod. Phys.* 23 (1951), pp. 69–89.

[129] L. Thomas. “The calculation of atomic fields.” In: *Proc. Cam. Phil. Soc.* 23 (1927), 542–548.

[130] E. Fermi. “A statistical Method for Determining some Properties of the Atoms and its Application to the Theory of the periodic Table of Elements”. In: *Z. Phys.* 48 (1928), 73–79.

[131] P. Dirac. “Note on exchange phenomena in the Thomas atom”. In: *Proc. Cam. Phil. Soc.* 26 (1930), 376–385.

[132] P. Hohenberg and W. Kohn. “Inhomogeneous Electron Gas”. In: *Phys. Rev. B* 136 (1964), B864–&.

[133] W. Kohn and L. J. Sham. “Self-Consistent Equations Including Exchange and Correlation Effects”. In: *Phys. Rev.* 140 (1965), 1133–&.

[134] R. O. Jones and O. Gunnarsson. "The density functional formalism, its applications and prospects". In: *Rev. Mod. Phys.* 61 (1989), pp. 689–746.

[135] K. Burke. "Perspective on density functional theory". In: *J. Chem. Phys.* 136, 150901 (2012), p. 150901.

[136] S. Boys and F. Bernardi. "The calculation of small molecular interactions by the differences of separate total energies. Some procedures with reduced errors." In: *Mol. Phys.* 19 (1970), pp. 553–566.

[137] J. P. Perdew. "Density functional theory and the band gap problem". In: *Int. J. Quantum Chem.* 28 (1985), pp. 497–523.

[138] J. P. Perdew and A. Zunger. "2 Theorems on the Self-Interaction in Density Functional Theory". In: *Bull. Am. Phys. Soc.* 26 (1981), p. 470.

[139] R. Stowasser and R. Hoffmann. "What Do the Kohn-Sham Orbitals and Eigenvalues Mean?" In: *J. Am. Chem. Soc.* 121 (1999), pp. 3414–3420.

[140] A. Savin, C. Umrigar, and X. Gonze. "Relationship of Kohn-Sham eigenvalues to excitation energies". In: *Chem. Phys. Lett.* 288 (1998), pp. 391–395.

[141] J. Harris. "Adiabatic-connection approach to Kohn-Sham theory". In: *Phys. Rev. A* 29 (1984), pp. 1648–1659.

[142] M. Ernzerhof. "Construction of the adiabatic connection". In: *Chem. Phys. Lett.* 263 (1996), pp. 499–506.

[143] K. Burke, M. Ernzerhof, and J. P. Perdew. "The adiabatic connection method: a non-empirical hybrid". In: *Chem. Phys. Lett.* 265 (1997), pp. 115–120.

[144] J. Paier et al. "Screened hybrid density functionals applied to solids". In: *J. Chem. Phys.* 124, 154709 (2006), p. 154709.

[145] J. P. Perdew, M. Ernzerhof, and K. Burke. "Rationale for mixing exact exchange with density functional approximations". In: *J. Chem. Phys.* 105 (1996), pp. 9982–9985.

[146] A. D. Becke. "A new mixing of Hartree-Fock and local density-functional theories". In: *J. Chem. Phys.* 98 (1993), pp. 1372–1377.

[147] J. Heyd, G. E. Scuseria, and M. Ernzerhof. "Hybrid functionals based on a screened Coulomb potential". In: *J. Chem. Phys.* 118 (2003), pp. 8207–8215.

[148] J. Heyd and G. E. Scuseria. "Efficient hybrid density functional calculations in solids: Assessment of the Heyd-Scuseria-Ernzerhof screened Coulomb hybrid functional". In: *J. Chem. Phys.* 121 (2004), pp. 1187–1192.

[149] E. Runge and E. K. U. Gross. "Density-Functional Theory for Time-Dependent Systems". In: *Phys. Rev. Lett.* 52 (1984), pp. 997–1000.

[150] M. Marques and E. Gross. "Time-Dependent Density Functional Theory". In: *Annu. Rev. Phys. Chem.* 55 (2004), pp. 427–455.

[151] F. Karlický, R. Zbořil, and M. Otyepka. "Band gaps and structural properties of graphene halides and their derivates: A hybrid functional study with localized orbital basis sets". In: *J. Chem. Phys.* 137, 034709 (2012),

[152] R. Krishnan et al. "Self-consistent molecular orbital methods. XX. A basis set for correlated wave functions". In: *J. Chem. Phys.* 72 (1980), pp. 650–654.

[153] T. H. Dunning. "Gaussian-Basis Sets for use in Correlated Molecular Calculations .1. The Atoms Boron Through Neon and Hydrogen". In: *J. Chem. Phys.* 90 (1989), pp. 1007–1023.

[154] W. J. Hehre, R. Ditchfield, and J. A. Pople. "Self-Consistent Molecular Orbital Methods. XII. Further Extensions of Gaussian-Type Basis Sets for Use in Molecular Orbital Studies of Organic Molecules". In: *J. Chem. Phys.* 56 (1972), pp. 2257–2261.

[155] L. Valenzano et al. "Ab Initio Study of the Vibrational Spectrum and Related Properties of Crystalline Compounds; the Case of $CaCO_3$ Calcite". In: *Z. Phys. Chem.* 220 (2006), pp. 893–912.

[156] A. Nicolaï et al. "Molecular Dynamics Simulations of Graphene Oxide Frameworks". In: *J. Chem. Theory Comput.* 9 (2013), pp. 4890–4900.

[157] C. G. Broyden. "The Convergence of a Class of Double-rank Minimization Algorithms 1. General Considerations". In: *IMA J.Appl. Math.* 6 (1970), pp. 76–90.

[158] R. Fletcher. "A New Approach To Variable Metric Algorithms". In: *Comp. J.* 13 (1970), 317–&.

[159] D. Goldfarb. "A Family Of Variable-metric Methods Derived By Variational Means". In: *Math. Comp.* 24 (1970), 23–&.

[160] D. F. Shanno. "Conditioning Of Quasi-Newton Methods For Function Minimization". In: *Math. Comp.* 24 (1970), 647–&.

[161] H. J. Monkhorst and J. D. Pack. "Special points for Brillouin-zone integrations". In: *Phys. Rev. B* 13 (1976), pp. 5188–5192.

[162] D. G. Anderson. "Iterative procedures for nonlinear integral equations". In: *J. Assoc. Comput. Mach.* 12 (1965), pp. 547–560.

[163] P. Salvador et al. "On the effect of the BSSE on intermolecular potential energy surfaces. Comparison of a priori and a posteriori BSSE correction schemes". In: *Journal of Computational Chemistry* 22.7 (2001), pp. 765–786.

[164] S. Tomić et al. "Electronic and Optical Structure of Wurtzite $CuInS_2$". In: *J. Phys. Chem. C* 118 (2014), pp. 14478–14484.

[165] L. Bernasconi et al. "First-principles optical response of semiconductors and oxide materials". In: *Phys. Rev. B* 83 (2011), p. 195325.

[166] M. Lundie and S. Tomić. "Ab initio parameterisation of the 14 band k·p Hamiltonian: Zincblende study". In: *J. Phys. Conf. Ser.* 526 (2014), p. 012004.

[167] I. Vurgaftman, J. R. Meyer, and L. R. Ram-Mohan. "Band parameters for III-V compound semiconductors and their alloys". In: *J. Appl. Phys.* 89 (2001), pp. 5815–5875.

[168] C. Gómez-Navarro, M. Burghard, and K. Kern. "Elastic Properties of Chemically Derived Single Graphene Sheets". In: *Nano Lett.* 8 (2008), pp. 2045–2049.

[169] M. Lundie, Ž. Šljivančanin, and S. Tomić. "Analysis of energy gap opening in graphene oxide". In: *J. Phys. Conf. Ser.* 526 (2014), p. 012003.

[170] Q. Peng et al. "Mechanical degradation of graphene by epoxidation: insights from first-principles calculations". In: *Phys. Chem. Chem. Phys.* 17 (2015), pp. 19484–19490.

[171] J. Cao, H.-J. Yin, and R. Song. "Circular dichroism of graphene oxide: the chiral structure model". In: *Front. Mater. Sci.* 7 (2013), pp. 83–90.

[172] F. Xia et al. "Two-dimensional material nanophotonics". In: *Nat. Photon.* 8 (2014), pp. 899–907.

[173] M. Lundie, Ž. Šljivančanin, and S. Tomić. "Electronic and optical properties of reduced graphene oxide". In: *J. Mater. Chem. C* 3 (2015), pp. 7632–7641.

[174] D. Kozawa et al. "Excitonic Photoluminescence from Nanodisc States in Graphene Oxides". In: *J. Phys. Chem. Lett.* 5 (2014), pp. 1754–1759.

[175] K.-H. Wu et al. "Electron-beam writing of deoxygenated micro-patterns on graphene oxide film". In: *Carbon* 95 (2015), pp. 738–745.

[176] H. Shi et al. "Tuning the nonlinear optical absorption of reduced graphene oxide by chemical reduction". In: *Opt. Express* 22 (2014), pp. 19375–19385.

[177] S. Grimme. "Semiempirical GGA-type density functional constructed with a long-range dispersion correction". In: *J. Comput. Chem.* 27 (2006), pp. 1787–1799.

Appendices

A

M-CC-PCVDZ BASIS SET FOR CARBON

6 8
0 0 8 2.0 1.0
6665.0000000 0.0006920
1000.0000000 0.0053290
228.0000000 0.0270770
64.7100000 0.1017180
21.0600000 0.2747400
7.4950000 0.4485640
2.7970000 0.2850740
0.5215000 0.0152040
0 0 8 2.0 1.0
6665.0000000 -0.0001460
1000.0000000 -0.0011540
228.0000000 -0.0057250
64.7100000 -0.0233120
21.0600000 -0.0639550
7.4950000 -0.1499810
2.7970000 -0.1272620
0.5215000 0.5445290
0 0 1 0.0 1.0
0.1596000 1.0000000
0 0 1 0.0 1.0
4.5300000 1.0000000
0 2 3 2.0 1.0
9.4390000 0.0381090
2.0020000 0.2094800

0.5456000 0.5085570
0 2 1 0.0 1.0
0.1785000 1.0000000
0 2 1 0.0 1.0
14.5570000 1.0000000
0 3 1 0.0 1.0
0.5500000 1.0000000

B

CC-PCVDZ BASIS SET FOR OXYGEN

8 8
0 0 8 2.0 1.0
11720.0000000 0.0007100
1759.0000000 0.0054700
400.8000000 0.0278370
113.7000000 0.1048000
37.0300000 0.2830620
13.2700000 0.4487190
5.0250000 0.2709520
1.0130000 0.0154580
0 0 8 2.0 1.0
11720.0000000 -0.0001600
1759.0000000 -0.0012630
400.8000000 -0.0062670
113.7000000 -0.0257160
37.0300000 -0.0709240
13.2700000 -0.1654110
5.0250000 -0.1169550
1.0130000 0.5573680
0 0 1 0.0 1.0
0.3023000 1.0000000
0 0 1 0.0 1.0
8.2150000 1.0000000
0 2 3 4.0 1.0
17.7000000 0.0430180
3.8540000 0.2289130

1.0460000 0.5087280
0 2 1 0.0 1.0
0.2753000 1.0000000
0 2 1 0.0 1.0
26.0560000 1.0000000
0 3 1 0.0 1.0
1.1850000 1.0000000

C

POB-TZVP BASIS SET FOR HYDROGEN

1 4
0 0 3 1.0 1.0
34.061341000 0.00602519780
5.1235746000 0.04502109400
1.1646626000 0.20189726000
0 0 1 0.0 1.0
0.4157455100 1.00000000000
0 0 1 0.0 1.0
0.1795111000 1.00000000000
0 2 1 0.0 1.0
0.8000000000 1.00000000000